



THE UNIVERSITY *of* EDINBURGH

Edinburgh Research Explorer

MIGHTEE-HI: The HI emission project of the MeerKAT MIGHTEE survey

Citation for published version:

Maddox, N, Frank, BS, Ponomareva, AA, Jarvis, MJ, Adams, EAK, Davé, R, Oosterloo, TA, Santos, MG, Blyth, SL, Glowacki, M, Kraan-Korteweg, RC, Mulaudzi, W, Namumba, B, Prandoni, I, Rajohnson, SHA, Spekkens, K, Adams, NJ, Bowler, RAA, Collier, JD, Heywood, I, Sekhar, S & Taylor, AR 2021, 'MIGHTEE-HI: The HI emission project of the MeerKAT MIGHTEE survey', *Astronomy and Astrophysics*, vol. 646, A35, pp. 1-14. <https://doi.org/10.1051/0004-6361/202039655>

Digital Object Identifier (DOI):

[10.1051/0004-6361/202039655](https://doi.org/10.1051/0004-6361/202039655)

Link:

[Link to publication record in Edinburgh Research Explorer](#)

Document Version:

Peer reviewed version

Published In:

Astronomy and Astrophysics

General rights

Copyright for the publications made accessible via the Edinburgh Research Explorer is retained by the author(s) and / or other copyright owners and it is a condition of accessing these publications that users recognise and abide by the legal requirements associated with these rights.

Take down policy

The University of Edinburgh has made every reasonable effort to ensure that Edinburgh Research Explorer content complies with UK legislation. If you believe that the public display of this file breaches copyright please contact openaccess@ed.ac.uk providing details, and we will remove access to the work immediately and investigate your claim.



MIGHTEE-HI: The H I emission project of the MeerKAT MIGHTEE survey[★]

Natasha Maddox¹, Bradley S. Frank^{2,3,4}, A. A. Ponomareva⁵, M. J. Jarvis^{5,6}, E. A. K. Adams^{7,8}, R. Dave^{9,6,10}, T. A. Oosterloo^{7,8}, M. G. Santos^{6,2}, S. L. Blyth⁴, M. Glowacki¹¹, R. C. Kraan-Korteweg⁴, W. Mulaudzi⁴, B. Namumba¹², I. Prandoni¹³, S. H. A. Rajohnson⁴, K. Spekkens¹⁴, N. J. Adams⁵, R. A. A. Bowler⁵, J. D. Collier^{3,15}, I. Heywood^{5,12,2}, S. Sekhar^{3,16}, and A. R. Taylor^{3,11}

¹ Faculty of Physics, Ludwig-Maximilians-Universität, Scheinerstr. 1, 81679 Munich, Germany
e-mail: natasha.maddox@gmail.com

² South African Radio Astronomy Observatory, 2 Fir Street, Observatory, 7925, South Africa

³ The Inter-University Institute for Data Intensive Astronomy (IDIA), and University of Cape Town, Private Bag X3, Rondebosch, 7701, South Africa

⁴ Department of Astronomy, University of Cape Town, Private Bag X3, Rondebosch 7701, South Africa

⁵ Oxford Astrophysics, Denys Wilkinson Building, University of Oxford, Keble Rd, Oxford, OX1 3RH, UK

⁶ Department of Physics and Astronomy, University of the Western Cape, Robert Sobukwe Road, Bellville 7535, South Africa

⁷ ASTRON, the Netherlands Institute for Radio Astronomy, Oude Hoogeveensedijk 4, 7991 PD Dwingeloo, The Netherlands

⁸ Kapteyn Astronomical Institute, PO Box 800, 9700 AV Groningen, The Netherlands

⁹ Institute for Astronomy, University of Edinburgh, EH9 3HJ, UK

¹⁰ South African Astronomical Observatory, PO Box 9, Observatory, 7935, South Africa

¹¹ The Inter-University Institute for Data Intensive Astronomy (IDIA), and University of the Western Cape, Robert Sobukwe Road, Bellville 7535, South Africa

¹² Department of Physics and Electronics, Rhodes University, PO Box 94, Makhanda, 6140, South Africa

¹³ INAF - Istituto di Radioastronomia, Via P. Gobetti 101, 40129 Bologna, Italy

¹⁴ Department of Physics and Space Science, Royal Military College of Canada, PO Box 17000, Station Forces, Kingston, Ontario, Canada K7K 7B4

¹⁵ School of Science, Western Sydney University, Locked Bag 1797, Penrith, NSW 2751, Australia

¹⁶ National Radio Astronomy Observatory, 1003 Lopezville Road, Socorro, NM 87801, USA

Received October 13, 2020; accepted November 10, 2020

ABSTRACT

We present the H I emission project within the MIGHTEE survey, currently being carried out with the newly commissioned MeerKAT radio telescope. This is one of the first deep, blind, medium-wide interferometric surveys for neutral hydrogen (H I) ever undertaken, extending our knowledge of H I emission to $z = 0.6$. The science goals of this medium-deep, medium-wide survey are extensive, including the evolution of the neutral gas content of galaxies over the past 5 billion years. Simulations predict nearly 3000 galaxies over $0 < z < 0.4$ will be detected directly in H I, with statistical detections extending to $z = 0.6$. The survey allows us to explore H I as a function of galaxy environment, with massive groups and galaxy clusters within the survey volume. Additionally, the area is large enough to contain as many as 50 local galaxies with H I mass $< 10^8 M_{\odot}$, which allows us to study the low-mass galaxy population. The 20 deg² main survey area is centred on fields with exceptional multi-wavelength ancillary data, with photometry ranging from optical through far-infrared wavelengths, supplemented with multiple spectroscopic campaigns. We describe here the survey design and the key science goals. We also show first results from the Early Science observations, including kinematic modelling of individual sources, along with the redshift, H I, and stellar mass ranges of the sample to date.

Key words. surveys–galaxies:evolution–galaxies:star formation–galaxies:kinematics and dynamics–radio lines: galaxies

1. Introduction

The neutral hydrogen (H I) content of galaxies serves as the raw material for the build-up of stellar mass. It is therefore essential that this component be incorporated into our multi-wavelength census of galaxy evolution. Unlike the stellar mass, the H I content of galaxies is a non-monotonic quantity, with gas being accreted, expelled, re-accreted, stored, and consumed. As such, we would like to observe the H I in galaxies as a function of cosmic time. Until recently, this was hindered by technological limita-

tions. Radio telescopes with small bandwidth restricted observations to narrow redshift ranges. The intrinsic faintness of the H I signal coupled with the limited sensitivity of existing facilities meant that regular observations extending beyond the local Universe were out of reach.

Several large-area surveys have been undertaken to detect H I in the low-redshift ($z < 0.1$) Universe. In the Southern Hemisphere, the H I Parkes All-Sky Survey (HIPASS; Barnes et al. 2001), complemented by the Northern HIPASS extension (NHICAT; Wong et al. 2006) and the Effelsberg Bonn H I Survey (EBHIS; Kerp et al. 2011) in the north, cover the entire sky. The Arecibo Legacy Fast ALFA Survey (ALFALFA; Giovanelli et al.

[★] Raw data available at <https://archive.sarao.ac.za>

2005) provides improved spatial resolution and sensitivity over 6900 deg^2 . These large-area surveys were performed blindly over their limited bandwidth and are invaluable as they provide the benchmark for the $z = 0$ cosmic H I density (Jones et al. 2018a).

At higher redshifts, targeted surveys such as the Blind Ultra-Deep H I Environmental Survey (BUDHIES; Verheijen et al. 2007; Jaffé et al. 2013) and the HIGHz survey (Catinella & Cortese 2015) spent many hundreds of hours of observations to detect individual galaxies at $z \sim 0.2$. While providing the first look at H I in galaxies at cosmological distances, the targets were chosen in advance based on their optical properties, thus they are not necessarily representative of the general galaxy population.

Technological advances, aided by increased computing capacity, are enabling the next generation of radio telescopes to explore previously inaccessible parameter space, undertaking blind H I surveys spanning substantial redshift ranges. The number of new H I-focused surveys indicates the importance of these observations for our understanding of galaxy evolution. The recently upgraded Karl G. Jansky Very Large Array (VLA) has the bandwidth in the L-band to observe the H I spectral line simultaneously from redshift zero to $z \sim 0.42$. The COSMOS H I Large Extragalactic Survey (CHILES) is exploiting this expanded frequency range to be the first next-generation deep H I survey, having already acquired the highest redshift direct H I detection to date, at $z = 0.376$ (Fernández et al. 2016). At lower frequencies, the upgraded Giant Metrewave Radio Telescope (uGMRT) has recently produced statistical H I detections at $z \sim 0.3$ (Bera et al. 2019) and has the frequency coverage to detect H I to $z \sim 1$ via statistical methods.

With a much-expanded field of view (FoV) relative to its predecessor, the APERTURE Tile in Focus (Apertif; Verheijen et al. 2008; Oosterloo et al. 2009) phased array feed system now deployed on the Westerbork Synthesis Radio Telescope (WSRT) upgrades the existing facility to a wide-field survey instrument. The imaging surveys underway include a wide and a medium-deep tier, designed to cover 3500 and 350 deg^2 , respectively, in the full survey plan, with spectral coverage for H I to $z = 0.26$ (Adams & van Leeuwen 2019; Hess et al. in prep.).

The next generation of newly built facilities, employing new technologies, further open parameter space that has eluded existing instrumentation. The Australian Square Kilometre Array Pathfinder (ASKAP; Johnston et al. 2008) employs a new Phased Array Feed (PAF) receiver design, similar in concept to Apertif, to provide 30 deg^2 of instantaneous coverage. This large FoV will enable the Widefield ASKAP L-band Legacy All-sky Blind survey (WALLABY; Koribalski et al. 2020) to observe the entire Southern Sky, providing increased redshift sensitivity and much-improved spatial resolution over the existing HIPASS data. The Deep Investigation of Neutral Gas Origins (DINGO; Meyer 2009) survey provides the corresponding deep and ultra-deep tiers, spending several thousands of hours integrating to detect H I to $z \sim 0.4$ over tens of square degrees.

1.1. MeerKAT

Observing H I over large areas covering cosmological ranges in redshift is one of the key science goals of the Square Kilometre Array (SKA; Braun et al. 2015), and is within the capabilities of the SKA precursor facility MeerKAT (Jonas & MeerKAT Team 2016). The 64-dish array, equipped with L-band ($900 < \nu < 1670 \text{ MHz}$), UHF-band ($580 < \nu < 1015 \text{ MHz}$) and higher frequency S-band ($1750 < \nu < 3500 \text{ MHz}$) receivers, is

the most sensitive centimetre-wavelength interferometer in the Southern Hemisphere, only to be surpassed by the SKA. Although MeerKAT employs a single-pixel feed rather than a PAF, the 13.5-m offset Gregorian dishes provide a $>1 \text{ deg}^2$ field-of-view (FoV) at 1420 MHz (i.e. $z = 0$ for H I observations), $\sim 4\times$ larger than the FoV for the VLA. The system equivalent flux density (SEFD) of the MeerKAT dish operating at L-band has been measured and found to be similar to the larger (25-m) VLA dishes at similar frequencies, due to MeerKAT's much lower system temperature (Jonas & MeerKAT Team 2016). The factor of ~ 2 increase in number of dishes, 64 for MeerKAT compared to 27 for VLA, thus reduces observing time to achieve a given flux limit by a factor of four. Combining the increased sensitivity and larger FoV, the survey speed of MeerKAT is approximately 16 times that of the VLA at L-band. The distribution of antennas simultaneously provides good angular resolution ($\sim 10 \text{ arcsec}$) while retaining sensitivity to low surface brightness and extended features. A stunning example of the performance of the array and quality of the data is the image of the Galactic Centre in radio continuum (Heywood et al. 2019).

A combination of depth and area coverage are essential to fully parametrise the H I Universe. Sensitivity is required to detect the intrinsically faint H I signals, both from nearby low-mass objects, and more distant higher-mass galaxies. As H I is known to be sensitive to galactic environments, large volumes are required to fully sample a range of environments at a given redshift, including galaxies in the field. Therefore, MeerKAT is the ideal instrument with which to undertake a deep, extragalactic, large-area (tens-thousands of square degrees), blind H I survey.

MeerKAT will undertake eight Large Survey Projects (LSPs) before the SKA begins operations. Several LSPs have significant H I focus, indicating the advances in this field MeerKAT will bring. The MeerKAT H I Observations of Nearby Galactic Objects; Observing Southern Emitters survey (MHONGOOSE; de Blok et al. 2016) focuses on nearby, well-resolved galaxies, detecting the neutral gas to low column densities that probe the connection between galaxies and the intergalactic medium. The MeerKAT Fornax Survey (MFS; Serra et al. 2016) is centred on the nearby Fornax cluster, investigating the H I in galaxies within this dense and dynamic environment. Looking At the Distant Universe with the MeerKAT Array (LADUMA; Blyth et al. 2016) will spend thousands of hours of integration on a single pointing to give the deepest view of the H I universe, extending to $z = 1.4$. Also extending to high redshifts is the MeerKAT Absorption Line Survey (MALS; Gupta et al. 2016), looking instead to detect H I in absorption towards background radio continuum sources.

Here we describe the MeerKAT International Giga-Hertz Tiered Extragalactic Exploration survey (MIGHTEE; Jarvis et al. 2016) LSP, focusing on the H I science enabled within the survey. In Sect. 2, we describe the details of the survey, along with predicted galaxy number counts. In Sect. 3, we outline the key science goals of the project. In Sect. 4, we outline the data products that will be delivered and provide illustrative examples. Section 5 gives a summary of the work. Concordance cosmology with $H_0 = 67.4 \text{ km s}^{-1} \text{ Mpc}^{-1}$ (thus $h \equiv H_0/100 \text{ km s}^{-1} \text{ Mpc}^{-1} = 0.674$), $\Omega_m = 0.315$, $\Omega_\Lambda = 0.685$ is assumed (Planck Collaboration et al. 2018), and AB magnitudes are used throughout unless otherwise stated.

2. Survey description

The parent survey for this project is the MeerKAT International GigaHertz Tiered Extragalactic Exploration survey (MIGHTEE;

Jarvis et al. 2016). MIGHTEE is one of eight guaranteed-time LSPs to be undertaken with MeerKAT. The survey will cover 20 deg² divided over four fields (see Table 1). The nominal integration time per MeerKAT pointing is ~16 hours, but due to overlap within the mosaic pointings, the effective integration time for points within the mosaic increases to ~23 hours. The continuum confusion floor with a 6–8 arcsec synthesised beam at ~1000 MHz is reached with integrations longer than this. Full-depth continuum imaging has yielded a confusion-limited image with a thermal noise floor of ~2 μJy beam⁻¹, in line with the survey design predictions. The actual observing strategy may evolve from this nominal plan as the survey progresses.

The MIGHTEE collaboration is organised into working groups that focus on radio continuum, H I in emission, H I in absorption, and polarisation. The working groups closely collaborate as there is substantial overlap between the data products and respective science cases.

2.1. MIGHTEE-HI

The MeerKAT data are collected in spectral line mode, so the MIGHTEE survey is a fully commensal continuum, polarisation, and spectral line project. The key metrics for the H I science to be undertaken with MIGHTEE, hereafter designated as MIGHTEE-HI, are listed in Table 2.

To maximise scientific return from MeerKAT observations, the MeerKAT Fornax Survey (Serra et al. 2016) and MIGHTEE have agreed that the volume behind the Fornax cluster will be analysed as part of MIGHTEE. The division between the two surveys is set to be at 110 Mpc, corresponding to $z = 0.025$, or $\nu = 1385$ MHz, and increases the effective area of MIGHTEE-HI to 32 deg² (see Table 1). The MFS mosaic pattern is slightly more closely packed than for the MIGHTEE survey, with an effective integration time of 25 hours per sky location, thus the per-channel noise level for MFS and MIGHTEE-HI will be comparable.

MIGHTEE-HI is strongly complementary with other next-generation emission-line surveys. In particular, the planned DINGO Deep tier will cover 150 deg² over $0 < z < 0.26$ while the Ultradeep tier extends to $0.1 < z < 0.43$ over 60 deg². MIGHTEE-HI covers half the area of the Ultradeep tier, but with greater sensitivity, better spatial resolution and higher maximum redshift. The Apertif medium-deep survey is comparable to the DINGO Deep tier, focusing on the Northern Hemisphere.

The ultra-deep CHILES project has 1000 hours of integration of a single pointing with the VLA in B configuration, and has better spatial resolution (~5 arcsec at 1420 MHz) than MeerKAT, but lower sensitivity to extended structures (Jarvis et al. in prep.). The expected sensitivity of CHILES at 1420 MHz, ~50 μJy beam⁻¹ per 31 kHz channel (Fernández et al. 2016), is a factor of two deeper than the ~100 μJy beam⁻¹ sensitivity per 26 kHz channel for MIGHTEE-HI. However, the area covered is only 0.25 deg², significantly smaller than the 32 deg² contained within MIGHTEE. The MeerKAT LSP LADUMA is conceptually similar to CHILES, spending thousands of hours of integration on a single pointing, but employs both the L- and UHF-bands to extend the sensitivity to H I to $z = 1.4$. LADUMA takes advantage of MeerKAT's increasing FoV with redshift to encompass more volume, ranging from ~1 deg² at $z = 0$ to >5 deg² at the highest redshift. MIGHTEE and LADUMA are complementary in area and depth, as illustrated in Sect. 3.1.

While MIGHTEE-HI, and indeed any of the deep or ultra-deep surveys, cannot compete in area covered with the wide-area surveys such as WALLABY, they do contain substantial

cosmological volumes. The volume contained within 32 deg² and $0 < z < 0.58$ is 0.033 Gpc³, almost three times that of the HIPASS survey, which surveyed $\delta < 2$ and $z < 0.0423$. MIGHTEE-HI also extends 2.5 Gyr of cosmological lookback time farther than WALLABY.

In full survey mode, MIGHTEE is being observed with a spectral resolution of 26 kHz, corresponding to 5.5 km s⁻¹ channels at $z = 0$. The MeerKAT 64-dish array consists of a compact core, with 70 per cent of the dishes contained within a diameter of approximately 1.5 km, and the remaining dishes distributed out to a maximum baseline of 7.7 km. The array configuration produces optimal sensitivity behaviour between resolutions of 8–80 arcsec at 1420 MHz (Jonas & MeerKAT Team 2016). Spectral line imaging based on MIGHTEE observations shows that using a Briggs robustness parameter of 0.5 produces a nominal resolution of ~12 arcsec.

The raw visibility data is converted to Measurement Set (MS) format, and is transferred from the MeerKAT archive to the Ilifu cluster¹ hosted at the University of Cape Town. Prior to calibration, we flag three frequency ranges corresponding to bands of persistent radio frequency interference (RFI), at 933–960 MHz, 1163–1310 MHz, and 1524–1630 MHz. Once flagged, the data is further split into multi measurement sets (MMSs) corresponding to 50 MHz windows. The full-Stokes *a priori* or cross calibration is done using the IDIA processMeerKAT pipeline² (Collier et al., in prep.); each spectral window is processed concurrently. Bandpass calibration is done using either J1939-6342 or J0408-6546. The secondary calibrator is used to solve for antenna-dependent gains, leakages and antenna XY phase. At the end of cross-calibration, the MMSs are reassembled and self-calibration is done on the downsampled data (averaged by a factor of four). Three loops of phase-only gain calibration is done for each observation, and the resulting solutions are applied to the full resolution data using linear interpolation in time and frequency.

The first step in continuum subtraction involves the subtraction of the final model generated by the self-calibration process. Polynomial fits to the visibility data are subtracted in the second step, for each spectral window. Spectral line imaging is performed on the resulting data. A final step of median filtering is done on the output image cubes, in order to reduce any remaining artefacts due to direction-dependent errors. See Frank et al. (in prep.) for a full description of the data reduction procedure.

For an effective integration time of 23.4 hours, 26 kHz channels, and the system equivalent flux density (SEFD) from the MeerKAT public documentation³, we expect to reach a sensitivity of ~100 μJy beam⁻¹ per channel at 1420 MHz. At an angular resolution of 12 (30) arcsec, the corresponding 3-σ column density sensitivity limits for MIGHTEE-HI are 1.3×10^{19} (2.0×10^{18}) cm⁻² at spectral resolution of 26 kHz, and 2.6×10^{19} (4.0×10^{18}) cm⁻² over 104 kHz, or 22 km s⁻¹, channels. The bulk of the H I mass associated with the main disk in galaxies is typically at $> 1.25 \times 10^{20}$ cm⁻², well within the sensitivity of the observations. The different science cases outlined in Sect. 3 benefit from data products at optimised spatial and spectral resolutions.

¹ <http://www.ilifu.ac.za/>

² <https://idia-pipelines.github.io>

³ <http://public.ska.ac.za/meerkat/meerkat-schedule>
Version release 2016-10-10

Table 1. List of the four fields within the MIGHTEE footprint. The fifth field is the MeerKAT Fornax Survey field, providing an additional 12 deg² of area beyond $z = 0.025$. The areas are computed at 1420 MHz, but become larger as the MeerKAT FoV increases with decreasing frequency. ^aA single pointing in the centre of ECDFS is covered by the LADUMA survey, surrounded by the MIGHTEE pointings. See Jarvis et al. (2016) for details.

Field Name	Area (deg ²) Full Survey	Centre Coordinates
COSMOS	2	10h01m, +02d12m
XMMLSS	8	02h20m, -04d50m
ECDFS ^a	8	03h32m, -28d00m
ELAIS-S	2	00h40m, -44d00m
MFS	12	03h38m, -35d27m

Table 2. Key parameters of the MIGHTEE-HI observations

Area covered	32 deg ²
Frequency range	900–1420 MHz
Redshift range for H I	$0 < z < 0.58$
Nominal angular resolution	12 arcsec
Velocity resolution	5.5 km s ⁻¹ (1420 MHz)
Per channel flux sensitivity	100 μJy beam ⁻¹ (1420 MHz)
Column density sensitivity (22 km s ⁻¹)	2.6×10^{19} cm ⁻²

2.2. Expected number counts

We can predict the approximate number of galaxies we expect to detect within MIGHTEE-HI, and their mass and redshift distribution, from upgraded simulations based on those from Maddox, Jarvis, & Oosterloo (2016). Briefly, we assume the H I mass function (HIMF) from Jones et al. (2018a) for the full ALFALFA survey, and we conservatively do not allow this to evolve with redshift. For a representative galaxy profile 150 km s⁻¹ wide, the per-channel sensitivity of $\sigma = 100 \mu\text{Jy beam}^{-1}$ translates to a 5- σ detection level of $0.075 \text{ Jy km s}^{-1} \text{ beam}^{-1}$. We note that this value is too large for low-mass galaxies, as they have H I profile widths substantially narrower than 150 km s⁻¹, thus the number of these galaxies predicted to be detected by the simulations is an underestimate. A more careful approach to the detection predictions for low-mass galaxies is taken in Sect. 3.4. We also note that the simulations here are strictly flux-limited, rather than surface-brightness limited. For example, a resolved galaxy can be below the per-beam flux limit, but if it is spatially resolved, it can still be detected. As described in Sect. 3.2, the majority of H I-detected galaxies beyond the local Universe will not be well-resolved, so this issue is minor and the results of the simulations are still illustrative. The effects of cosmic variance are ignored.

In the top panel of Fig. 1, the predicted number of detected galaxies as a function of redshift for 32 deg² is shown, with galaxies directly detected to $z \sim 0.4$. While the MeerKAT L-band spans 900–1670 MHz, resulting in sensitivity to H I over $0 < z < 0.58$, radio frequency interference (RFI) from global navigation satellite systems (GNSS) at 1164–1300 MHz, which corresponds to $0.09 < z < 0.22$ for H I, affects the data quality in that frequency range. RFI from GNSS is seen at all radio observatories, and thus affects all H I observations at those frequencies. The hatched region in Fig. 1 corresponds to the frequency range most affected by RFI. In the ideal case with no RFI, we expect to detect ~ 1750 galaxies to be individually detected in the main 20 deg² MIGHTEE-HI area, with an extra > 1000 galax-

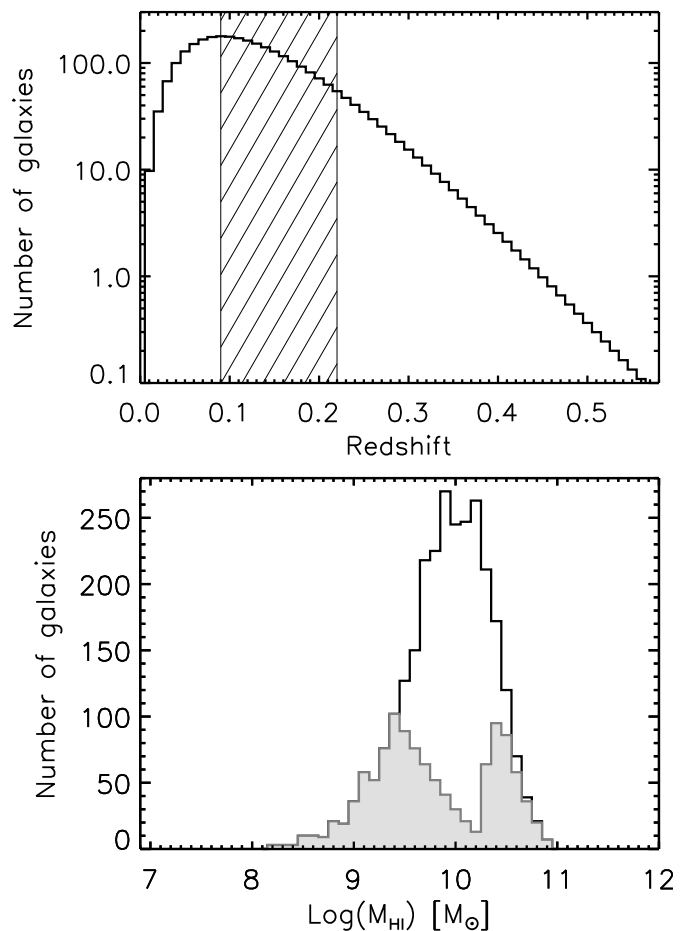


Fig. 1. Conservative number of galaxies expected from the full 32 deg² of MIGHTEE-HI area, derived from simulations. (Top) Expected number of galaxies from 32 deg² as a function of redshift. The redshift range most affected by RFI is hatched out. (Bottom) Expected number of galaxies from 32 deg² as a function of M_{HI} . The solid-line histogram is the distribution covering the full redshift range, whereas the light filled histogram represents the worst-case of fully excluding the redshift range hatched out in the top panel.

ies in the 12 deg² MeerKAT Fornax Survey area. In the most pessimistic case, excluding the frequency range affected by RFI entirely, these numbers drop to lower limits of 730 in the main area and 420 in the Fornax area. In practice, there are narrow frequency ranges that are less affected than others and can be salvaged. RFI is also less prominent at increasingly long baselines, so removing data from short baselines, while accepting the associated loss in sensitivity, is another method for alleviating the issue. See Figure 7 in Mauch et al. (2020) for a MeerKAT L-band spectrum illustrating the RFI environment, and the benefit gained by removing short baselines.

The bottom panel of Fig. 1 shows the expected distribution of H I mass (M_{HI}) of galaxies within the 32 deg² MIGHTEE-HI area. The solid-lined histogram includes galaxies across the full redshift range, whereas the light-filled histogram corresponds to the worst-case scenario of assuming no useful data can be recovered from the redshift range $0.09 < z < 0.22$, and therefore represents a lower limit. Advancing RFI identification and mitigation techniques currently underway will clearly have a large beneficial effect on H I observations undertaken at these frequencies, including for future SKA surveys.

2.3. Ancillary data

The four fields central to MIGHTEE listed in Table 1 are some of the most well-studied extragalactic fields accessible from the Southern Hemisphere and are covered by various surveys ranging from the X-ray through far-infrared wavelengths. While long integrations are required to detect the most distant objects, the resulting depth is also valuable for low-redshift galaxies, revealing details not visible in lower quality imaging, as illustrated in Fig. 2. The redshift of the galaxy, $z = 0.0055$, is known from the H I detection, and would be difficult to obtain from optical spectroscopy due to its intrinsic faintness and low surface brightness.

A tabulated description of the data sets available in XMM-LSS, ECDFS and ELAIS-S1, across all wavelengths, can be found in Table 1 of Chen et al. (2018), and the data available in the COSMOS field is generally greater in extent⁴. The key data sets for the H I science described here are the optical photometry from Canada-France-Hawaii-Telescope Legacy Survey (CFHTLS) and HyperSuprimeCam (HSC; Aihara et al. 2018, 2019). The near-infrared data are from the VISTA Deep Extragalactic Observations (VIDEO; Jarvis et al. 2013) and the VISTA Extragalactic Infrared Legacy Survey (VEILS; Höning et al. 2017), which together cover the MIGHTEE XMM-LSS, ECDFS and ELAIS-S1 fields, while UltraVISTA (McCracken et al. 2012) covers the COSMOS field. These data have been matched in pixel-space and catalogues have been made, providing photometry based on a range of apertures as described in Bowler et al. (2020), alongside photometric redshift catalogues (Adams et al. 2019). A source catalogue derived using ProFound (Robotham et al. 2018) to obtain accurate photometry for the low redshift, large angular size galaxies detected in H I within the deep imaging data will also be available (Davies et al. in prep.; Adams et al. in prep.).

The fields are also being covered by past, current and future spectroscopic campaigns. Past surveys include the VIMOS VLT Deep Survey (VVDS; Le Fèvre et al. 2013), VANDEL (McLure et al. 2018; Pentericci et al. 2018), Z-COSMOS (Lilly et al. 2009), the Sloan Digital Sky Survey Data Release 12 (SDSS-DR12; Alam et al. 2015), 3D-HST (Skelton et al. 2014; Momcheva et al. 2016), the PRISM MULTI-object Survey (PRIMUS; Coil et al. 2011; Cool et al. 2013), DEIMOS-10K (Hasinger et al. 2018) and the Fiber Multi-object Spectrograph (FMOS) COSMOS Survey (Silverman et al. 2015). Many of these large, extragalactic spectroscopic surveys target the high-redshift Universe, beyond the reach of H I surveys.

Three programmes, one ongoing and two soon to start, seek to collect more complete data over the redshift range $0 < z < 1$. The Deep Extragalactic Visible Legacy Survey (DEVILS, Davies et al. 2018) is an ongoing survey being carried out with the multi-object spectrograph on the Anglo-Australian Telescope (AAT), within the COSMOS, XMM-LSS and ECDFS fields. The target redshift range is $0.3 < z < 1.0$, aiming for very high (95 per cent) completeness to $Y < 21.2$, and will be a key data set for MIGHTEE-HI science, in particular for stacking, as outlined in Sect. 3.7. In the coming years, DEVILS will be complemented by surveys with the Multi-Object Optical Near-Infrared Spectrograph (MOONS; Cirasuolo et al. 2014) and the Wide-Area VISTA Extragalactic Survey (WAVES; Driver et al. 2019) with the 4-m Optical Spectroscopic Telescope (4MOST; de Jong et al. 2019). WAVES aims for 90 per cent completeness to $z < 0.8$ and $Z < 21.25$ within the 4 primary MIGHTEE fields, probing below the characteristic stellar mass over the full redshift range. The high completeness and stellar mass-based se-

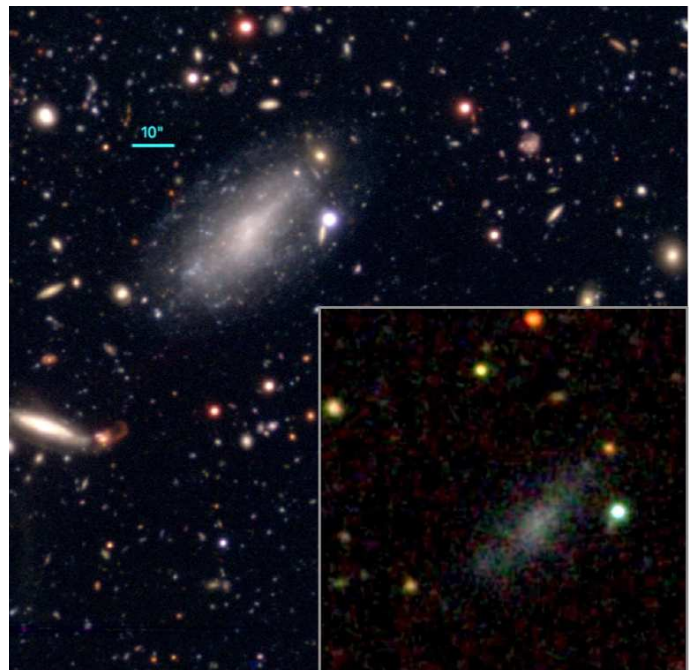


Fig. 2. HSC *gri* false-colour image of a galaxy at $z = 0.0055$ detected within MIGHTEE-HI, with the SDSS *gri* image on the same size scale inset. The depth and image quality of the HSC images reveal structural details and low surface brightness features not visible in shallower imaging.

lection will alleviate biases from galaxy type and small-scale galaxy environment. We also note that these deep surveys are complemented by spectroscopy from the SDSS in both COSMOS and XMM-LSS, and the all-sky 2MASS Redshift Survey (2MRS; Huchra et al. 2012), which provide useful spectroscopic information on the bright, low-redshift galaxy population.

These fields will also be covered by the Vera C. Rubin Observatory as part of the deep drilling fields (Jones et al. 2013), providing extremely deep visible wavelength imaging, and the wide- and deep-survey to be carried out with the EUCLID satellite (Laureijs et al. 2010), providing deep and high-resolution near-infrared imaging.

The MFS area has recently been observed with the VLT Survey Telescope (VST), providing imaging in the SDSS *u*, *g*, *r* and *i* bands, with surface brightness sensitivity extending to $27\text{--}28$ mag arcsec⁻² (Venhola et al. 2018). Spectroscopy over the full field, including existing and new observations, has been compiled by Maddox et al. (2019). Imaging in 5 optical bands from the Dark Energy Survey (DES; Flaugher 2005) also covers the MFS area.

3. Key science goals

There are a number of key science goals to be addressed with the MIGHTEE-HI data, which take advantage of the unique combination of depth, area and available ancillary data. Below is a list of the primary science topics to be addressed.

3.1. The H I mass function

A headline goal of the MIGHTEE-HI project is the determination of the HIMF, as a function of redshift. This fundamental quantity describes the distribution of H I within galaxies. The most recent constraints on the $z \sim 0$ HIMF parameters, includ-

⁴ <http://cosmos.astro.caltech.edu>

ing the low-mass slope, the characteristic mass, and the normalisation, come from the ALFALFA survey (Jones et al. 2018a). This work, covering 6900 deg² and containing more than 25,000 sources, illustrates the effects of large-scale structure and sample variance on the HIMF determination, particularly on the low-mass slope.

Instead of wide-area and shallow, the Arecibo Ultra-Deep Survey (AUDS; Hoppmann et al. 2015) used deep integrations with the Arecibo telescope over a smaller area to detect 102 galaxies over 1.35 deg². This extended the HIMF parametrisation to the mean redshift of their sample at $z = 0.065$.

While predicted to contain an order of magnitude fewer sources than ALFALFA, MIGHTEE-HI extends to higher redshifts, affording us a first opportunity to investigate the HIMF as a function of redshift to $z = 0.1$ and beyond. LADUMA is also aiming to constrain the HIMF at $z > 0$. In Fig. 3, the parameter space is divided into cells $\Delta z = 0.01$ and $\Delta \log(M_{\text{HI}}) = 0.1$, and shows where MIGHTEE-HI and LADUMA are expected to directly detect galaxies. For MIGHTEE-HI, the light grey shaded region indicates cells within which at least one galaxy is predicted to be detected by the simulations, medium grey shading is 10 galaxies per cell, and dark grey is 25 galaxies per cell. In reality, the shaded regions do not have sharp edges, primarily due to inclination effects that have not been accounted for, but the simulations are still useful for illustration. For LADUMA, the light, medium and dark red shaded regions indicate cells with at least 1, 4 and 8 galaxies predicted by the simulations. LADUMA in fact employs both the L- and UHF-bands on MeerKAT, extending sensitivity to H I to $z = 1.4$, but we show only the redshift range covered by the L-band here.

From Fig. 3, MIGHTEE-HI and LADUMA probe complementary parameter space in H I mass, thus the combination of the two surveys will enable parametrisation of the HIMF to $z \sim 0.3$ using direct detections, and higher redshifts using statistical techniques. In particular, the characteristic H I mass is well covered by MIGHTEE-HI at $z < 0.15$. Below the formal detection threshold, a statistical approach to determining the HIMF using MIGHTEE-HI data can also be employed, as in Pan et al. (2020). This technique will exploit the relatively large volume probed by MIGHTEE-HI at $0.2 < z < 0.6$.

Integration of the HIMF provides a measure of the cosmic H I gas density, Ω_{HI} . A compilation from Rhee et al. (2018) (see their Figure 14) shows an increasing number of measurements of Ω_{HI} at low and intermediate redshifts. However, care must be used when interpreting this collection of results. Density measurements from directly detected H I extend to $z < 0.127$, with the highest redshift determination from AUDS (Hoppmann et al. 2015). Beyond that, to $z \sim 0.4$, results are derived from statistical methods, primarily H I stacking experiments. At $z > 0.4$, it is H I in absorption towards background quasars being measured. With MIGHTEE-HI, coupled with the LADUMA survey, Ω_{HI} can be measured from directly detected H I to at least $z = 0.3$, and possibly beyond. Statistical methods can be used to $z = 0.58$, which overlaps in redshift with the Ω_{HI} probes derived from H I absorption. We will thus, for the first time, have independent measures of Ω_{HI} , one from H I emission, and one from H I absorption, at overlapping redshifts.

3.2. Kinematics from spatially resolved H I

Resolved galaxies in the local Universe have been extensively studied in the past. The main scientific topics based on resolved H I can be summarised in two broad categories. First, the study of galaxy gas accretion and depletion, which includes minor merg-

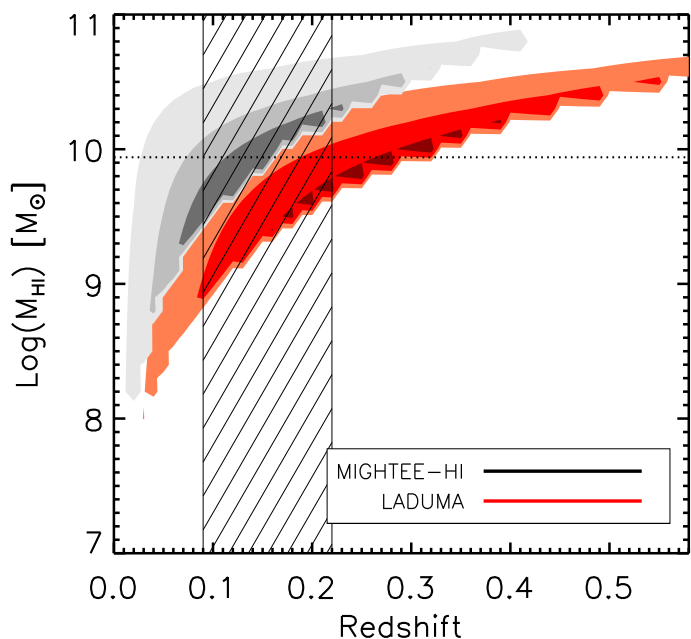


Fig. 3. M_{HI} – redshift parameter space, showing where MIGHTEE-HI and LADUMA are sensitive to galaxies, divided into cells of size $\Delta z = 0.01$ and $\Delta \log(M_{\text{HI}}) = 0.1$. Light, medium, and dark grey shading indicates where at least one, 10, and 25 galaxies are expected per cell. Light, medium, and dark red shading shows where at least one, four, and eight galaxies are expected per cell. The horizontal dotted line indicates the $z = 0$ characteristic H I mass from the HIMF. The hatched region corresponds to the redshift range $0.09 < z < 0.22$ most affected by RFI.

ers (e.g. Di Teodoro & Fraternali 2014), hot-mode accretion (e.g. Heald et al. 2011; Marasco et al. 2019), ram-pressure stripping (e.g. Jaffé et al. 2015; Yoon et al. 2017), outflows and feedback (e.g. Bagetakos et al. 2011; Maccagni et al. 2017). This is further expanded in Sect. 3.6. Second, the study of galaxy structure and kinematics, which includes warps and lopsidedness (e.g. van der Kruit 2007), rotation curves and dark matter (e.g. Ponomareva, Verheijen & Bosma 2016; Aniyan et al. 2018), angular momentum (e.g. Obreschkow et al. 2016; Posti et al. 2018), non-circular motions (e.g. Shetty, Ostriker & Vogel 2008). Though these topics are scientifically vast, almost all take advantage of kinematic modelling.

Figure 4 illustrates the mass and redshift range of MIGHTEE-HI galaxies that will be spatially resolved for kinematic modelling. The grey shading is the same as in Fig. 3. The well-established relation between the H I mass of a galaxy and its diameter, D_{HI} , as recently investigated by Wang et al. (2016), can be used to predict how many galaxies within MIGHTEE-HI will be resolved. Assuming a MeerKAT beam major axis of 12 arcsec, this is converted to a linear size in kiloparsecs as a function of redshift, and then converted to an equivalent M_{HI} . The M_{HI} corresponding to the MeerKAT beam size is shown as the black curve in Fig. 4.

Kinematic modelling requires at least three resolution elements (with the signal-to-noise ratio of the data larger than 2-3) across the major axis of a galaxy in order to constrain the dynamics of the gas (Di Teodoro & Fraternali 2015). The M_{HI} corresponding to three times the MeerKAT beam is shown as the red dashed line in Fig. 4, and we refer to this as minimally resolved. The blue dotted line corresponds to 5 MeerKAT beams across a galaxy, which is generally the requirement for a galaxy to be considered well-resolved. We expect ~ 200 galaxies to be minimally resolved out to $z < 0.09$, with up to 50 being well resolved. No

galaxies will be even minimally resolved at $z > 0.22$ using the expected 12 arcsec beam, but different weightings could be used to increase the resolution at the expense of sensitivity. Thus, with ≈ 150 – 200 resolved galaxies out to $z < 0.09$, MIGHTEE-HI will provide a large homogeneous sample beyond the local Universe, which will significantly contribute to the above-mentioned studies. Additional information can be gained from the shape of the resolved H I spectral profile (Watts et al. 2020).

The other caveat for kinematic modelling is the initial estimates of the geometry of the disk, that is, the estimates of the position and inclination angles. While current kinematic modelling software is able to blindly predict the systemic velocity or the position of the centre of a galaxy, as well as locate an object in the data cube, the results will be unrealistic if an inaccurate initial estimation of the position and/or inclination angle is given. However, the ancillary photometric data available to MIGHTEE-HI will enable initial estimates of the disk geometry.

As an example of a well-resolved galaxy, Fig. 5 shows the position-velocity diagram of NGC 895 using data from MIGHTEE-HI, and its kinematic model produced using the 3^{D} Barolo software (Di Teodoro & Fraternali 2015). The synthesised beam for these observations is 11×9 arcsec, while the galaxy is 280 arcsec across the major axis. Within the modelling, the separation between the points on the rotation curve is 10 arcsec, therefore we model one data point of rotation curve per synthesised beam, and the galaxy is ~ 28 beams across the major axis. The resulting rotation velocity of this galaxy is $V_{\text{rot}} = \pm 165 \text{ km s}^{-1}$, which is consistent with the previous measurements of the same galaxy from the VLA observations (Pisano, Wilcots & Liu 2002).

Initial tests suggest that smaller galaxies can also be successfully modelled with 3^{D} Barolo. The galaxy shown in Fig. 6 is at $z = 0.061$, and with an H I diameter of 45 arcsec, only spans 3 resolution elements across its major axis. The synthesised beam here is 14.5×11 arcsec. Within 3^{D} Barolo, two points of rotation curve per beam were requested, resulting in a rotation curve with points separated by 5 arcsec. Initial estimates of the galaxy inclination and position angles were derived from the optical photometry, but kept as free parameters within the modelling. The resulting rotational velocity of the galaxy at the outer most point of the rotation curve is $V_{\text{out}} = 123 \text{ km s}^{-1}$, in good agreement with the rotational velocity measured at the full-width half maximum (FWHM) of the integrated line profile ($V_{\text{rot}} = 127 \text{ km s}^{-1}$), corrected for inclination and random motions.

3.3. The Tully-Fisher relation

The dynamical scaling relations of disk galaxies exhibit tight correlations between the main galaxy properties: size, mass, and rotational velocity. Among these is the Tully-Fisher relation (TFR, Tully & Fisher 1977), and the baryonic TFR, linking the baryonic content of a galaxy to its rotational velocity (McGaugh et al. 2000; Ponomareva et al. 2018; Lelli et al. 2019). Moreover, the TFR holds over a wide wavelength range (Ponomareva et al. 2017) and in various environments (Willick 1999). It has also been studied extensively in the theoretical framework of galaxy formation and evolution (Vogelsberger et al. 2014; Schaye et al. 2015), as the success of any particular theory depends on its ability to reproduce the statistical properties of the TFR such as slope, scatter and the zero point.

MIGHTEE-HI will provide a unique opportunity to study the statistical properties of the TFR homogeneously at various wavelengths. The spectroscopic ancillary data will be of great

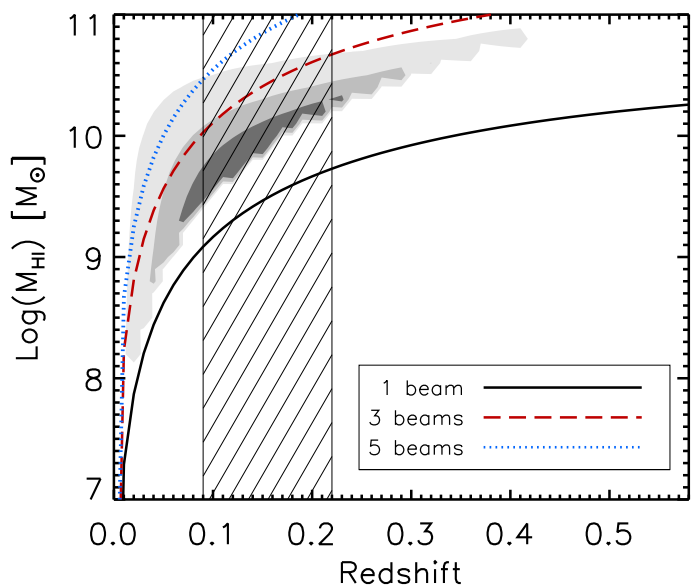


Fig. 4. M_{HI} – redshift parameter space, showing where MIGHTEE-HI is sensitive to galaxies, divided into cells of size $\Delta z = 0.01$ and $\Delta \log(M_{\text{HI}}) = 0.1$. Light, medium, and dark grey shading indicates where at least one, 10, and 25 galaxies are expected per cell. The black, red, and blue curves correspond to the M_{HI} of galaxies as a function of redshift, for three fixed diameters, using the $M_{\text{HI}} - D_{\text{HI}}$ relation from Wang et al. (2016). The black line shows the 12 arcsec MeerKAT beam, indicating galaxies below this mass will be unresolved. The red dashed line is for marginally resolved sources and the blue dashed line is for well-resolved sources with five beams across. $0.09 < z < 0.22$ is worst-affected by RFI, and the size and shape of the synthesised beam is strongly affected in this region.

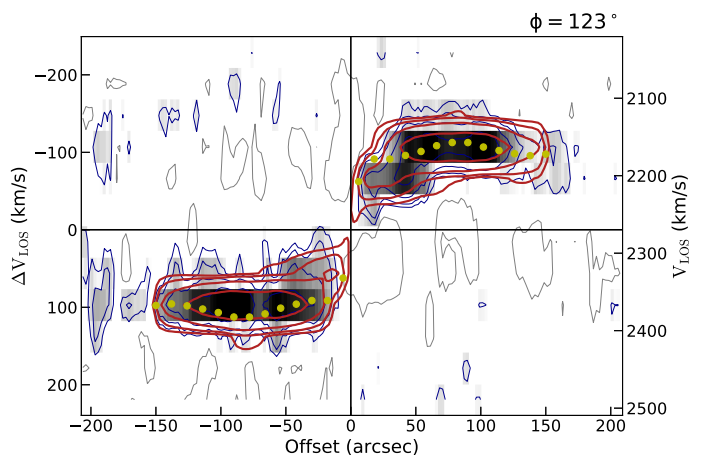


Fig. 5. Position-velocity diagram of NGC 895, using H I data from MIGHTEE-HI, is shown in grey scale and blue contours. The 3D kinematic model made with 3^{D} Barolo (Di Teodoro & Fraternali 2015) is shown with red contours, and the resulting rotation curve of the galaxy, projected on the data, is shown with yellow dots.

importance to reduce the scatter associated with the distance uncertainty. Moreover, MIGHTEE-HI is a volume-limited, blind survey encompassing various galactic environments. This will reduce any selection bias that might be present in targeted studies.

Comparing the TFR at different redshifts is a powerful tool to constrain galaxy growth. Significant evolution in the TFR would suggest an imbalance in the accretion histories and mass assembly of dark matter and baryons. At low redshifts, H I, resolved

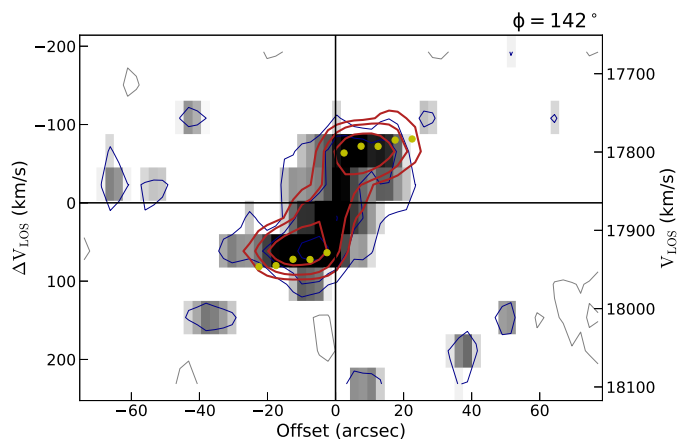


Fig. 6. Position-velocity diagram of a smaller galaxy detected within MIGHTEE-HI, showing that kinematic modelling can be performed successfully when the galaxy is only marginally resolved, with three resolution elements across the major axis. The MIGHTEE-HI data are shown in grey scale and blue contours, while the 3D kinematic model is in red contours, and the resulting rotation curve is shown with yellow dots.

rotation curves and/or the velocity width of the H I line are used as the kinematic tracer, as they provide the best measure of the total gravitational potential of a galaxy by extending far beyond the optical radius into the dark matter halo. However, to date H I has remained undetectable in emission beyond the local Universe. Carbon monoxide (CO) has been used as the kinematic tracer at higher redshifts (Topal et al. 2018), but its distribution is known to be compact and may not probe the dark matter halo potential. The same applies to H α and [O III] lines, which are also used as kinematic tracers for the TFR studies at higher redshifts (e.g. Übler et al. 2017; Tiley et al. 2019). Moreover, current studies are not conclusive as there is no strong agreement about the presence or absence of the evolution of the TFR. Thus, MIGHTEE-HI, in combination with LADUMA, will allow us to study the H I TFR in redshift bins up to $z \sim 0.4$ using direct detections and statistical methods (see Sect. 3.7), and compare it to the relation using galaxies selected, and with velocities measured, in a consistent way.

3.4. H I in low-mass galaxies

Dwarf galaxies can provide critical tests of our cosmological model, and are excellent laboratories for studying the processes that control galaxy formation. Indeed, these two areas of study are inherently connected as many of the noted discrepancies between observations of dwarf galaxies and predictions from Λ CDM simulations are resolved when the galaxy formation processes, notably the important role of star formation feedback, are accounted for (see review by Bullock & Boylan-Kolchin 2017).

H I observations offer a powerful tool for identifying isolated, gas-rich dwarf galaxies and for understanding those dwarf galaxies, including their internal kinematics and dark matter halo hosts. For example, several of the lowest-metallicity systems known in the Local Universe have been discovered via their H I emission (e.g. Skillman et al. 2013; Hirschauer et al. 2016), providing a local opportunity, where high spatial resolution can be achieved, to study star formation conditions similar to those in the early Universe. H I studies of extended, extremely low surface brightness dwarf galaxies (the so-called ultra-diffuse galaxy population), indicate that they do not fol-

low the canonical baryonic TFR and may have an unusual dark matter content (Leisman et al. 2017; Mancera Piña et al. 2019), testing our understanding of galaxy formation. Compilations of current H I observations and comparisons to Λ CDM simulations indicate that the kinematics of field dwarf galaxies are inconsistent with predictions for their expected hosting dark matter halos (Papastergis et al. 2015; Papastergis & Shankar 2016).

Dwarf galaxies have narrower velocity widths than more massive galaxies due to lower halo masses. Since H I detection limits depend on the width of the line, different mass galaxies have different detection limits. In order to predict the number of dwarf galaxies expected in the MIGHTEE footprint, we assume a typical velocity width of 30, 50 and 100 km s^{-1} for $M_{\text{HI}} < 10^7$, $10^7 - 10^8$, and $10^8 - 10^9 M_{\odot}$. In the MIGHTEE footprint, we expect to detect ~ 50 galaxies with $M_{\text{HI}} < 10^8 M_{\odot}$, and ~ 250 galaxies in the range $10^8 - 10^9 M_{\odot}$. The additional background Fornax volume starts around the detection limit for $10^8 M_{\odot}$, and adds ~ 100 additional galaxies in the mass range $10^8 - 10^9 M_{\odot}$. These predictions do not account for cosmic variance; given that dwarf galaxies can only be detected in limited, nearby volumes, these predictions are approximations only.

The resolved detections will display the true power of the MIGHTEE-HI data. As discussed in Sect. 3.2, at least three resolution elements are required to enable kinematic modelling. With a 12 arcsec beam, only a few galaxies below $10^9 M_{\odot}$ will be resolved. Re-imaging specific sources at higher angular resolution after detection at lower angular resolution will provide more resolved dwarf galaxies. For an 8 arcsec beam, there will be ~ 50 resolved galaxies below $10^9 M_{\odot}$. This is comparable in size to existing samples of dwarf galaxies in this mass range but would provide a blind, rather than targeted, sample. The derived rotation velocities will allow an optically unbiased view of the baryonic TFR at dwarf galaxy masses plus an examination of the ‘too-big-to-fail’ problem in the field (Papastergis et al. 2015; Papastergis & Shankar 2016).

The multi-wavelength ancillary data will allow galaxy formation processes to be studied in detail. The H I data provides the gas reservoir, plus a distance, enabling stellar masses and star formation rates to be derived. While MIGHTEE-HI will not provide the large numbers of dwarf galaxies that surveys such as WALLABY and the wide-area tier of the Apertif project will, the exceptional multi-wavelength data coverage and potential for higher spatial resolution will enable more detailed studies, complementing the work to be done with the wide-area H I surveys.

3.5. H I as a function of environment

The H I content of galaxies is a function of environment on a variety of scales. On the largest scales, Jones et al. (2018a) showed the effect of large-scale structure on the determination of the HIMF, with the largest effect seen at low H I masses. Splitting the full ALFALFA survey area into a ‘Spring’ region, containing the Virgo cluster and the Local Supercluster, and a ‘Fall’ region, containing a large void in front of the Perseus-Pisces supercluster, the faint end slope of the HIMF differs by more than $3\text{-}\sigma$. This illustrates the need to encompass a large cosmic volume.

Focusing directly on the Virgo cluster itself, the VLA H I Imaging survey of Virgo galaxies in Atomic gas (VIVA; Chung et al. 2009) looked at detailed H I properties of galaxies at a range of cluster-centric distances. Galaxies near the cluster centre were found to have small, truncated H I disks with respect to the sizes of their stellar disks, while galaxies at larger distances had asymmetric H I distributions, pointing away from the cluster centre. The MFS will extend this work, obtaining similar

data for the Fornax cluster in the Southern Hemisphere. While the MIGHTEE-HI survey volume does not contain clusters as massive as Virgo, it does contain 10–15 lower-mass clusters and galaxy groups per square degree (see, for example, the X-ray selected catalogue of Finoguenov et al. 2007 within the COSMOS region, and Finoguenov et al. 2010 and Adami et al. 2018 covering the XMM-LSS), providing a variety of environments to explore. At $z < 0.1$, as seen in Fig. 4, the resolution is sufficient to investigate the H I morphologies of the H I-massive galaxies. At higher redshifts, the integrated H I properties of galaxies, along with the spectrally resolved profiles, can be investigated in these different environments.

The group environment, while not as extreme as massive clusters, has also been shown to affect the H I content of galaxies, with group halo mass and location within the group (Hess & Wilcots 2013; Yoon & Rosenberg 2015; Odekon et al. 2016; Brown et al. 2017) influencing the amount of H I detected. This manifests as a flattening of the faint end slope of the HIMF (Pisano et al. 2011; Said, Kraan-Korteweg & Staveley-Smith 2019; Jones et al. 2020). It has also been found that cosmic structures such as filaments can affect the H I content of galaxies (Crone Odekon et al. 2018). The importance of large-area observations reaching beyond the nominal group extent is well illustrated in Serra et al. (2013), who find a tail of H I clouds containing $M_{\text{HI}} = 5 \times 10^8 M_{\odot}$ extending 40 arcmin, postulated to be the result of interactions between a gas-rich galaxy with the group potential.

Previous work studying H I in these environments has all been limited to $z \sim 0$ by the available data. With the deep imaging available over the full MIGHTEE footprint, along with highly complete spectroscopy, we will be able to identify the different galaxy environments, including clusters, groups and filaments, over the full redshift range of MIGHTEE-HI, and investigate the behaviour of H I as a function of environment over the past 5 billion years.

3.6. The interface between galaxies and the surrounding medium

In recent years, it has become clear that galaxies, and in particular star forming galaxies, cannot be isolated systems as far as their gas content is concerned. One main indication is that the timescale over which the star formation in a galaxy would consume all the gas in that galaxy is much shorter than a Hubble time (e.g. Bigiel et al. 2008). If there is no channel through which star forming galaxies acquire new gas, the present gas reservoirs would be depleted in only a few Gyr. Studies of our own Galaxy show that the disk stars have formed at a more or less constant rate for the last 12 Gyr (e.g. Schönrich & Binney 2009), which can only occur when the gas content of the Milky Way is also more or less constant. Chemical evolution models of the stellar abundances also indicate extensive and continuous accretion of fresh unpolluted gas (e.g. Chiappini, Matteucci & Romano 2001).

It is still unclear how star forming galaxies acquire fresh gas in order to maintain their star formation rate. However, there are several possibilities for how galaxies could be doing this. One obvious candidate is the accretion of gas-rich companions, while another option is that the accretion of gas structures similar to the Galactic High-Velocity Clouds plays an important role. This latter process could correspond to the so-called cold accretion, which is seen in modern numerical simulations of galaxy formation. Both types of accretion are observed in some nearby spiral galaxies, but the data suggest that the observed accre-

tion rates may not be sufficient to maintain star formation at current levels, unless the observed cold gas clouds that are accreting have significant ionised counterparts (Sancisi et al. 2008; Di Teodoro & Fraternali 2014; Putman, Peek & Joung 2012).

An alternative to accretion of external gas is that gas from the hot gaseous halo, which spiral galaxies are known to possess, cools and rains down onto the disk. This can help rebuild a substantial disk after an early merger of two disk galaxies (Athanasoula et al. 2016). Additionally, an interesting idea that has been proposed is that galactic fountains could play an important role in stimulating cooling of the hot halo gas (Fraternali & Binney 2008). The energy released by supernovae and stellar winds drives relatively cold gas flows into the gaseous halo where they interact with the hot, low-metallicity halo gas. The mixing of these two gas components drastically reduces the cooling time of the hot halo gas so that part of the halo gas cools and rains down onto the disk, adding to the existing gas reservoir. Observations have given indications that such an interface layer exists in at least some galaxies. Detailed H I observations of a small number of nearby galaxies (e.g. NGC 2403 Fraternali et al. 2001; NGC 891 Oosterloo, Fraternali & Sancisi 2007) and more recently the result from the HALOGAS survey (Heald et al. 2011), show that the thin H I disk of spiral galaxies is surrounded by a thicker H I disk, which possibly corresponds to the layer where the interaction between the galactic fountain and the halo occurs. These thick H I disks have different kinematics compared to the thin disks: They have lower rotation speeds and also display a small, inward motion (Marasco et al. 2019). These characteristics are consistent with the galactic fountain models.

However, sufficiently sensitive H I data that allow us to study gas accretion, and galactic fountains in detail, are available only for a small, not entirely representative sample of galaxies and there are still several important open questions. The HALOGAS sample from Marasco et al. (2019) only contains 15 galaxies and is the largest collection of homogeneously studied objects. The MIGHTEE-HI survey has the required sensitivity and resolution to increase the number of galaxies for which data are available. In particular, the galaxies will not be pre-selected, allowing a blind census of gas accretion and of the role of galactic fountains play.

3.7. H I below the detection limit

Science from MIGHTEE-HI is not restricted to direct detections of H I in galaxies. Statistical techniques can be employed to extract information from below the noise floor, to extend to lower H I masses and higher redshifts. The most common method for determining the average H I properties of an ensemble of galaxies is spectral stacking, where one relies on the existence of sufficiently accurate optical spectroscopy of the galaxies under investigation in order to align the H I spectra of a large number of non-detections, N , into a common reference frame, and then assume the noise of the co-added spectrum decreases as $N^{-1/2}$.

This has been successfully attempted over large areas (Delhaize et al. 2013), as a function of galaxy type (Brown et al. 2015), and as a function of stellar mass (Healy et al. 2019). Meyer et al. (2016) also showed the power of spectral stacking to recover the statistical properties of the TFR. Regions of the sky with either large numbers of galaxies, such as clusters (although these regions are biased by design) (Jaffé et al. 2016), or regions with particularly dense optical spectroscopic coverage (Rhee et al. 2016), are also good candidates for spectral stacking studies. The expanded frequency range of next-generation fa-

ilities enables H I detections to increasing redshifts (Bera et al. 2019). A new technique employing Bayesian statistics to model the distribution of fluxes from within a data cube has been shown to directly recover the HIMF from simulated data, rather than infer it from average values, extending below the formal noise limit (Pan et al. 2020). As described in Sect. 2.3, the MIGHTEE fields already have extensive optical spectroscopy, with more to come, which has been shown to be essential for the success of any stacking experiment (Maddox et al. 2013).

3.8. H I intensity mapping

Neutral hydrogen intensity mapping (H I IM) has been proposed as a new technique to probe the large-scale structure of the Universe and deliver precision constraints on cosmology (Bharadwaj, Nath & Sethi 2001; Battye, Davies & Weller 2004; Loeb & Wyithe 2008). The idea is to integrate all of the H I emission within a given pixel, of specified angular and frequency resolution. The advantage is that one can achieve higher sensitivity as we do not require a detection of individual galaxies (i.e. there is no threshold for detection). One of the main issues is to disentangle the desired signal from the smooth but strong foreground contaminants and instrumental effects (Wolz et al. 2014; Olivari et al. 2018).

Several experiments have been proposed in order to measure this signal, using single dish telescopes or interferometers (Bandura et al. 2014; Xu, Wang & Chen 2015; Newburgh et al. 2016; Santos et al. 2015). A precursor survey to the SKA with MeerKAT has also been proposed using the single dish measurements (Santos et al. 2017).

Measurements using the Green Bank Telescope produced the first tentative detection of the cosmological H I intensity signal by cross-correlating with the WiggleZ redshift survey (Chang et al. 2010; Switzer et al. 2013). More recently, a survey using the Parkes telescope made a detection in cross-correlation with the 2dF survey (Anderson et al. 2018) at $z < 0.098$. They measured an amplitude of the cross-power spectrum lower than expected from a dark matter power spectrum, assuming an H I bias and mass density equal to measurements from the ALFALFA survey (especially at $k \sim 1.5h/\text{Mpc}$). This indicates a possible lack of clustering or a small correlation coefficient with the optical galaxies that needs to be further investigated.

In addition to measuring the auto correlation, using the data from MIGHTEE, we plan to search for the H I IM signal in cross-correlation with optical galaxy catalogues, taking advantage of the excellent spectroscopic and photometric coverage of the survey fields. We note that such a detection would be a first for an interferometer.

Within a single MIGHTEE pointing, we will be able to probe scales between $0.3 \text{ Mpc}^{-1} < k < 20 \text{ Mpc}^{-1}$ (0.3 to 21 comoving Mpc) at $z \sim 0.27$, and using data from multiple MIGHTEE fields reduces the cosmic variance of the power spectrum. Although these scales are in the quasi-linear regime (i.e. smaller scales than the baryon acoustic oscillation window), they can still provide important cosmological constraints. Such measurements would provide a wealth of information for comparison with H I numerical simulations (e.g. Davé et al. 2019). In addition, these measurements will help constrain Ω_{HI} and, indirectly, the HIMF down to very low mass scales, for which a measurement of the shot noise will also help (e.g. Wolz, Blake & Wyithe 2017), and would not only include optically selected galaxies, but all the H I emission, irrespective of the galaxy with which it is associated.

3.9. Scaling relations

As the H I content of galaxies is a dynamic quantity, it is crucial that we are able to observe it as a function of cosmic time. The existing large-area surveys, such as HIPASS and ALFALFA, provide excellent $z = 0$ reference points for the current H I content of galaxies. The Analysis of the interstellar Medium in Isolated GALaxies project (AMIGA; Verdes-Montenegro et al. 2005) provides specific scaling relations at $z = 0$ derived from H I spectra as a reference for environmental effects (Jones et al. 2018b). With MIGHTEE, we have the opportunity to extend these observations to lookback times of up to 5 Gyr. With H I serving as one source of raw fuel for star formation, and thus the build-up of stellar mass, incorporating the neutral hydrogen component into our multi-wavelength census of galaxy evolution is essential.

The relation between the H I content of galaxies and their stellar mass at $z \sim 0$ is known to be non-linear, and a function of the dark matter halo parameters (Maddox et al. 2015). With MIGHTEE-HI, we can measure the H I mass of galaxies as both a function of stellar mass and redshift. The quality of the ancillary data available in the MIGHTEE footprint is essential, as it allows us to use statistical methods to probe scaling relations beyond where H I is directly detected, extending to higher redshifts and lower masses.

As MIGHTEE is a commensal spectral line and continuum survey, we have deep radio continuum images over the same area, from which we can measure star formation rates (SFRs) unaffected by dust obscuration, as well as active galactic nucleus (AGN) activity. Using the conservative $2\mu\text{Jy beam}^{-1}$ root mean square (RMS) for MIGHTEE, we can convert this to a $5\text{-}\sigma$ limiting SFR as a function of redshift using the relation from Murphy et al. (2011). At low redshifts, $z < 0.09$, very low SFRs are probed, down to $0.15 \text{ M}_{\odot} \text{ year}^{-1}$. At the high-redshift limit probed by H I $z \sim 0.58$, we are sensitive to $\text{SFR} \sim 10 \text{ M}_{\odot} \text{ year}^{-1}$.

3.10. H I in galaxy evolution simulations

The baryon cycling paradigm of galaxy evolution asserts that gas flows into and out of galaxies govern their evolution and properties (Somerville & Davé 2015). H I plays a key role in this by tracing gas around galaxies that is the reservoir of future star formation (Crain et al. 2017) as well as cool gas outflows (Faucher-Giguère et al. 2016). Numerical simulations of galaxy formation and evolution have shown that, even with many different choices for feedback models, it is possible to broadly reproduce observed stellar, star formation rate, and black hole properties over a range of redshifts (e.g. EAGLE, IllustrisTNG, and SIMBA; Schaye et al. 2015; Pillepich et al. 2018; Davé et al. 2019). However, the predicted properties of cold gas in and around galaxies vary widely, particularly in terms of their evolution (Davé et al. 2020).

MIGHTEE-HI will provide an unprecedented sample of observations for testing models at the present epoch out to intermediate redshifts. In particular, the large area will enable homogeneous environmental studies to better constrain the processes by which galaxies lose their H I within dense regions, which is important for quenching star formation in both central and satellite galaxies. Feedback and gas stripping processes, for instance, appear to be crucial for solving the too-big-to-fail problem (Verbeke et al. 2017; Oman et al. 2019a), and for predicting H I removal and consumption timescales in dense environments (e.g. Marasco et al. 2016; Rafieeantsoa, Davé & Naab 2019). Indeed, the suppression of H I likely extends into shock-

heated filamentary structures well outside groups and clusters (Wang et al. 2015; Rafieeerantsoa & Davé 2018), and the multi-wavelength data associated with MIGHTEE will be crucial for understanding the association of H I and star formation in the earliest stages of environmental quenching. Finally, the dynamical information provided by the high velocity resolution of MeerKAT will enable careful studies of the connection between galaxies and halos via the baryonic TFr (Sect. 3.3 and e.g. Glowacki, Elson, & Davé 2020).

It is becoming routine to generate H I data cubes from simulations including instrumental effects (e.g. MARTINI⁵; Oman 2019b), which will enable closer and more robust comparisons between both cosmological and zoom simulations, versus MIGHTEE-HI and ancillary data. Thus there is great potential for synergistic studies between cosmological hydrodynamical simulations and the H I studies of galaxies in the MIGHTEE-HI project, in order to constrain some of the most uncertain physical processes of galaxy formation associated with the baryon cycle.

4. Survey progress

Early Science observations with MeerKAT were undertaken from mid-2018 through mid-2019. For MIGHTEE, Early Science employs the full 64-dish array, but with limited spectral resolution, 208 kHz (44 km s^{-1} at $z = 0$) channels instead of 26 kHz (5.5 km s^{-1}) resolution. MIGHTEE has Early Science data for the COSMOS field, and three overlapping pointings within the XMMLSS field. There are three tracks (16 hours on source) for COSMOS, and two 8-hour tracks for each of the XMMLSS pointings (12 hours on source). Full science observations, with 26kHz spectral resolution, have commenced in 2020. The Early Science data have been reduced and spectral cubes generated. See Frank et al. (in prep.) for a full description of the MIGHTEE-HI Early Science Data.

4.1. Early Science

Within the restricted area observed in Early Science, there are already enough detections spanning a range of redshift and M_{HI} for population studies to begin, along with individual objects that warrant detailed attention. We highlight one of them here, to demonstrate the advantages of the MeerKAT instrument, and the discovery potential of the full survey.

As described in Sect. 3.2, several galaxies within MIGHTEE-HI will be well-resolved by MeerKAT. Figure 5 illustrates the kinematic modelling possible for such objects, while Fig. 6 shows that kinematic modelling can also be performed on galaxies that are only marginally resolved. The full investigation of the kinematics of MIGHTEE-HI Early Science galaxies is underway and will appear in future works. Figure 7 shows the total intensity, or moment 0, contours of NGC 895 overplotted on the HSC *grY* image. This one system illustrates several advantages of the high sensitivity, high-resolution MeerKAT data. Visible in Fig. 7 are not only the H I associated with the galaxy disk at $z = 0.0075$, but also tidal extensions, along with a dwarf companion also clearly detected. The mass of the main galaxy is $M_{\text{HI}} = 1.7 \times 10^{10} M_{\odot}$, similar to the $M_{\text{HI}} = 1.3 \times 10^{10} M_{\odot}$ found in Pisano, Wilcots & Liu (2002). The deep HSC imaging clearly shows the dwarf companion stellar counterpart, which had no catalogued redshift until the H I observations confirmed its association with the main galaxy. The companion mass is $M_{\text{HI}} = 5 \times 10^7 M_{\odot}$.

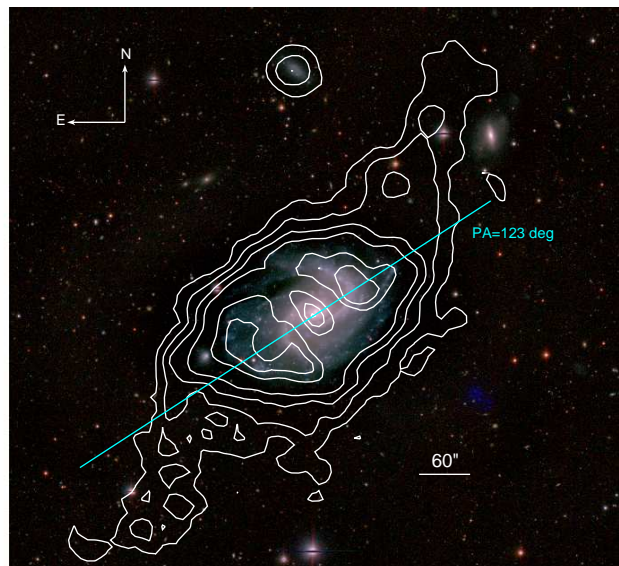


Fig. 7. MIGHTEE-HI H I total intensity contours, overplotted on the HSC *grY* image of NGC 895. Contours are at 1×10^{20} , 3×10^{20} , 6×10^{20} , 1×10^{21} , 2×10^{21} , and 2.5×10^{21} atoms cm^{-2} . The contours in the galaxy centre indicate a depression of H I, also seen in Fig. 5. The H I contours have been smoothed to 20×20 arcsec, and are based on ~ 12 hours of on-source integration. The scale-bar shows 60 arcsec, while the synthesised beam is 11×9 arcsec. The position angle from the modelling in Fig. 5 is marked in cyan.

4.1.1. Catalogue construction

With such a rich data set, and the large number of H I detections, the data will be collated within the MIGHTEE-HI working group into catalogues. In the first instance, source finding is performed visually and unguided, meaning no prior information about the location of galaxies is used. This will be supplemented by including automated source finding algorithms. We employ The Cube Analysis and Rendering Tool for Astronomy (CARTA⁶) for cube inspection. Cubes at multiple spatial and spectral resolutions can be created, according to specific science cases. For example, low-mass galaxies will require high spectral resolution to resolve the narrow line widths, whereas column density sensitivity for low surface brightness features can be enhanced at the expense of spatial resolution.

Once the position and frequency of each H I detection is known, cubelets around the sources are extracted from the cube. These cubelets are processed by the source finding and parameterisation tool SOFIA (Serra et al. 2015), where masks around emission in the relevant spectral channels are created. From these masks, the H I flux is summed, and the central frequency determined. With the relatively coarse spectral resolution of Early Science data, the central frequencies of galaxies are limited in precision, but will improve with full spectral resolution data. The H I flux combined with the emission frequency can be converted into an H I mass. Other data products of interest are the integrated H I line profiles, the width of the H I emission line at half the peak flux, W_{50} , the integrated flux map (moment 0) and velocity map (moment 1). These data products will all be made available first to the MIGHTEE-HI working group, and then publicly released after the data proprietary period has expired, via staged data releases coordinated across the MIGHTEE

⁵ <https://kyleaoman.github.io/martini/build/html/includem.html>, <https://cartavis.github.io/>

working groups. The Early Science Data Release will be mid-2021, with reduced data products hosted on the IDIA⁷ facility.

From the extensive ancillary data within the MIGHTEE survey footprint described in Sect. 2.3, several value-added quantities are available. The spectroscopic redshifts for all the H I sources are by definition given from the H I data themselves, as MIGHTEE is in fact a spectroscopic survey. This is particularly useful for the low-mass dwarf galaxies and low surface brightness galaxies, for which acquiring an optical redshift is difficult and thus these types of galaxies are often not targeted in optical surveys. If an optical spectrum also exists, the SFR can be derived directly from suitable emission lines, such as H α . Additionally, a dust-free estimate of the SFR can be derived from the MIGHTEE radio continuum map.

Using the available deep multi-wavelength optical and NIR imaging, we perform resolved photometry on the H I-detected galaxies. An elliptical aperture is determined for each galaxy individually, encompassing as much of the galaxy light as possible while excluding the light of foreground, background or neighbouring objects. The aperture is defined on the HSC *G*-band image and transferred directly to the CFHT *u*-band, HSC *riZY* bands, and NIR *JHKs* bands, and the aperture photometry extracted, resulting in 9-band photometry. Coupled with the accurate redshifts provided by the H I line, the photometry is fit by the spectral energy distribution (SED) fitting code *Le PHARE* (Arnouts et al. 1999; Ilbert et al. 2006) to produce stellar masses, star formation rates, and stellar ages. Thus, for each H I-selected source, we have coordinates, a spectroscopic redshift, and the H I properties of the galaxy, along with the optical properties of the stellar component, including stellar mass and star formation rate.

4.2. MIGHTEE-HI galaxies

While several individually detected galaxies warrant close investigation, the sample of H I-detected galaxies is already large enough to enable ensemble studies. Figure 8 shows the range of H I masses of galaxies visually detected in cubes as a function of redshift. The solid black line in the figure is the 5- σ flux limit from the simulations described in Sect. 2.2, altered to better represent the Early Science integration time and channel width, indicating the expected mass sensitivity limit as a function of redshift. The MIGHTEE-HI flux limit is a factor of ten deeper than the approximate flux limit of the large-area ALFALFA survey, shown as a red dashed curve, and extends further in redshift. Data at frequencies below 1310 MHz, corresponding to $z > 0.084$, have not yet been inspected and are not shown here. Isolated galaxies (i.e. not obvious satellites of larger galaxies) with M_{HI} as low as $10^7 M_{\odot}$ have been detected, in line with predictions. We expect the number of very low mass detections to increase with improved spectral resolution, as the intrinsic linewidths of these low-mass galaxies can be narrower than the Early Science 44 km s⁻¹ channels.

From the noise properties of the cubes, we can derive a measure of the statistical uncertainty on the H I masses of our individual objects. For each galaxy, the local RMS in emission-free regions is measured and converted to an H I mass error, assuming no uncertainty on the distance. At large masses, the uncertainty is ~ 5 per cent, and at lower masses, $\sim 10^8 M_{\odot}$, increases to approximately 20 per cent. The uncertainty typical for a low-mass galaxy is illustrated by the error bars on one point in the top left corner of Fig. 8.

Environmental studies benefit from the large FoV of MeerKAT. Galaxy groups uncovered in the Early Science data, as traced by their H I detections, span tens of arcminutes and fit easily into a single MeerKAT pointing. An overdensity is already apparent in Fig. 8 at $0.04 < z < 0.045$ within the XMMLSS field. At low redshift, $z \sim 0.04$, 60 arcmin corresponds to a physical scale of nearly 3 Mpc. At $z \sim 0.4$, the upper redshift limit of where we expect to directly detect H I, 60 arcmin corresponds to 19 Mpc, large enough to trace large-scale structure.

4.2.1. Scaling relations

The H I mass of the Early Science galaxies as a function of stellar mass is shown in Fig. 9. The H I-detected galaxies span 5 orders of magnitude in stellar mass, reaching $< 10^7 M_{\odot}$. The deeper optical imaging available within the MIGHTEE footprint allows us to probe lower stellar masses than ALFALFA, which relied on the shallower SDSS imaging. The low-mass end, below $M_{*} < 10^7 M_{\odot}$, is not yet well populated, but will become increasingly so as more area is surveyed.

The grey line in Fig. 9 traces the median relation derived from the 40% ALFALFA catalogue in bins of width $\text{Log}(M_{*})=0.4$, along with illustrative 1- σ uncertainties, as determined in Maddox et al. (2015). The red line traces the median relation derived from the 5 deg² of MIGHTEE-HI Early Science data, in bins of $\text{Log}(M_{*})=0.5$, also with illustrative 1- σ uncertainties. The deficit seen by the MIGHTEE-HI data at the high-mass end may be a result of the limited volume probed in Early Science. However, at intermediate masses, the MIGHTEE-HI and ALFALFA relations are in very good agreement. The apparent break at $M_{\text{HI}} \sim 10^9 M_{\odot}$ in this relation was first noted in the ALFALFA data (Maddox et al. 2015), and was not seen in HIPASS data, nor any galaxy simulations available. MIGHTEE-HI provides the first independent confirmation of the shape of the relation, employing data that extend a factor of ten deeper in H I mass. Studies of scaling relations illustrate the need for a combination of sensitivity, required to detect the low-mass systems, large area coverage of the MIGHTEE survey, to encompass a larger search volume, and the correspondingly deep optical and NIR imaging, to investigate the faint stellar counterparts.

5. Summary

The next generation of radio facilities are rapidly becoming operational, probing parameter space that has until recently remained largely unexplored. With the exceptional sensitivity of the SKA precursor MeerKAT, large-area surveys are able to reach unprecedented depths and redshifts. The MeerKAT MIGHTEE LSP is well underway, with several square degrees of Early Science data in hand. The survey design and scientific motivation for the H I component of the MIGHTEE LSP, designated as MIGHTEE-HI, are outlined here. A description of the data products that will be made available to the LSP, and ultimately, the global community is given, along with first science results highlighting the strengths of the survey. The combination of the new MeerKAT H I data, with the existing extensive multi-wavelength information available, provides a powerful resource for undertaking the science described in Sect. 3 and beyond. These new facilities are set to transform our view of the neutral gas component of galaxies, adding this crucial ingredient into our descriptions of galaxy formation and evolution. MeerKAT in particular, with its unprecedented combination of sensitivity, resolution, FoV, and bandwidth, is uniquely positioned to make great strides in H I science, well in advance of construction of the SKA.

⁷ <https://www.idia.ac.za/>

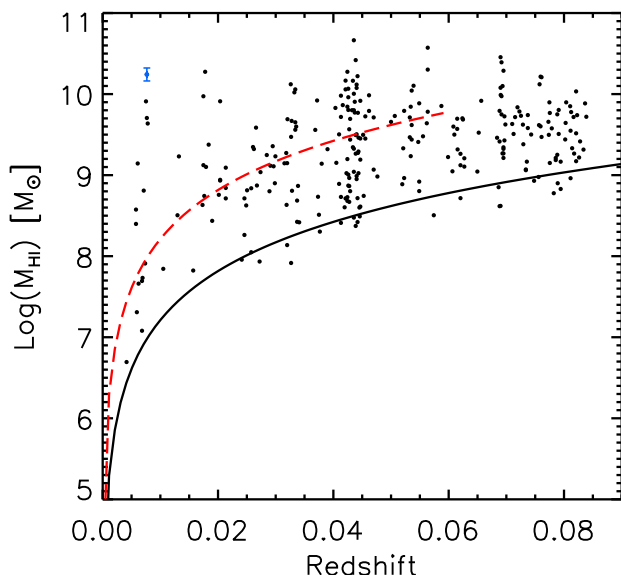


Fig. 8. HI masses as a function of redshift for the Early Science HI detections. Black points mark individual objects, while the curved black line indicates the $5\text{-}\sigma$ flux limit used for the simulations. An estimate of the uncertainty on the HI masses is illustrated for the blue point with error bars in the top left corner. The red dashed line is the approximate flux limit of the ALFALFA survey, which does not extend beyond $z \sim 0.06$. MIGHTEE-HI Early Science detections are found all the way to the upper redshift limit of $z = 0.084$.

Acknowledgements. We thank the referee, Prof Albert Bosma, for his careful reading of the manuscript and helpful comments which improved this paper. The authors gratefully acknowledge input from the MIGHTEE-HI working group for useful discussions and comments on early drafts of this paper. The MeerKAT telescope is operated by the South African Radio Astronomy Observatory, which

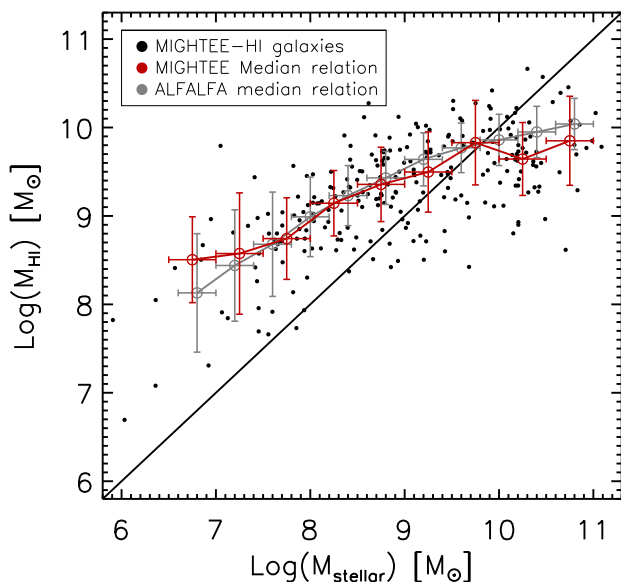


Fig. 9. HI masses as a function of stellar mass for MIGHTEE Early Science HI detections, spanning $0 < z < 0.84$. Black points mark individual objects. The curved red line indicates the median and $1\text{-}\sigma$ uncertainty of the relation from the MIGHTEE-HI points, while the grey line is the same relation derived from the ALFALFA survey (Maddox et al. 2015). The horizontal error bars indicate the width of the stellar mass bins.

is a facility of the National Research Foundation, an agency of the Department of Science and Innovation. We acknowledge use of the Inter-University Institute for Data Intensive Astronomy (IDIA) data intensive research cloud for data processing. IDIA is a South African university partnership involving the University of Cape Town, the University of Pretoria and the University of the Western Cape. The authors acknowledge the Centre for High Performance Computing (CHPC), South Africa, for providing computational resources to this research project. NM acknowledges support from the Bundesministerium für Bildung und Forschung (BMBF) D-MeerKAT award 05A2017. BSF, MJJ and IH would like to acknowledge support from the Africa-Oxford Visiting Fellows Programme. MJJ, AAP, RAAB and IH acknowledge support from the Oxford Hintze Centre for Astrophysical Surveys which is funded through generous support from the Hintze Family Charitable Foundation and the award of STFC consolidated grants (ST/S000488/1 and ST/N000919/1). NJA acknowledges funding from the Science and Technology Facilities Council (STFC) Grant Code ST/R505006/1. RAAB is supported by the Glasstone Foundation. EAKA is supported by the WISE research programme, which is financed by the Netherlands Organisation for Scientific Research (NWO). RD acknowledges support from the Wolfson Research Merit Award program of the U.K. Royal Society. MGS acknowledges support from the South African Radio Astronomy Observatory (SARAO) and the National Research Foundation (Grant No. 84156). IP acknowledges support from the Italian Ministry of Foreign Affairs and International Cooperation, Directorate General for the Country Promotion (Bilateral Grant Agreement ZA18GR02), and from the South African Department of Science and Technology's National Research Foundation (DST-NRF Grant Number 113121) as part of the ISARP RADIOSKY2020 Joint Research Scheme. RKK, SHAR and WM are supported through the South African Research Chairs Initiative of the Department of Science and Technology and National Research Foundation. This research has made use of NASA's Astrophysics Data System Bibliographic Services. This research made use of Astropy,⁸ a community-developed core Python package for Astronomy.

References

- Adami C., et al., 2018, *A&A*, 620, A5
 Adams E. A. K., van Leeuwen J., 2019, *NatAs*, 3, 188
 Adams N. J., et al., 2019, arXiv, arXiv:1912.01626
 Aihara H., et al., 2018, *PASJ*, 70, S4
 Aihara H., et al., 2019, *PASJ*, 71, 114
 Alam S., et al., 2015, *ApJS*, 219, 12
 Anderson C. J., et al., 2018, *MNRAS*, 476, 3382
 Aniyani S., et al., 2018, *MNRAS*, 476, 1909
 Arnouts S., Cristiani S., Moscardini L., Matarrese S., Lucchin F., Fontana A., Giallongo E., 1999, *MNRAS*, 310, 540
 Athanassoula E., Rodionov S. A., Peschken N., Lambert J. C., 2016, *ApJ*, 821, 90
 Bagetakos I., et al., 2011, *AJ*, 141, 23
 Bandura K., et al., 2014, *SPIE*, 9145, 914522, *SPIE*.9145
 Barnes D. G., et al., 2001, *MNRAS*, 322, 486
 Battye R. A., Davies R. D., Weller J., 2004, *MNRAS*, 355, 1339
 Bera A., Kanekar N., Chengalur J. N., Bagla J. S., 2019, *ApJL*, 882, L7
 Bharadwaj S., Nath B. B., Sethi S. K., 2001, *JApA*, 22, 21
 Bigiel F., Leroy A., Walter F., Brinks E., de Blok W. J. G., Madore B., Thornley M. D., 2008, *AJ*, 136, 2846
 de Blok W. J. G., et al., Proceedings of MeerKAT Science: On the Pathway to the SKA. 25-27 May, 7, mks.conf
 Blyth S., et al., 2016, Proceedings of MeerKAT Science: On the Pathway to the SKA. 25-27 May, 4, mks.conf
 Bowler R. A. A., et al., 2020, *MNRAS*, 493, 2059
 Braun R., Bourke T., Green J. A., Keane E., Wagg J., 2015, *Advancing Astrophysics with the Square Kilometre Array (AASKA14)*, 174
 Brown T., Catinella B., Cortese L., Kilborn V., Haynes M. P., Giovanelli R., 2015, *MNRAS*, 452, 2479
 Brown T., et al., 2017, *MNRAS*, 466, 1275
 Bullock J. S., Boylan-Kolchin M., 2017, *ARA&A*, 55, 343
 Catinella B., Cortese L., 2015, *MNRAS*, 446, 3526
 Chang T.-C., Pen U.-L., Bandura K., Peterson J. B., 2010, *Natur*, 466, 463
 Chen C.-T. J., et al., 2018, *MNRAS*, 478, 2132
 Chiappini C., Matteucci F., Romano D., 2001, *ApJ*, 554, 1044
 Chung A., van Gorkom J. H., Kenney J. D. P., Crowl H., Vollmer B., 2009, *AJ*, 138, 1741
 Cirasuolo M., et al., 2014, *SPIE*, 9147, 91470N, *SPIE*.9147
 Coil A. L., et al., 2011, *ApJ*, 741, 8
 Cool R. J., et al., 2013, *ApJ*, 767, 118
 Crain R. A., et al., 2017, *MNRAS*, 464, 4204

⁸ <http://www.astropy.org>

- Davé R., Anglés-Alcázar D., Narayanan D., Li Q., Rafieferantsoa M. H., Appleby S., 2019, *MNRAS*, 486, 2827
- Davé R., Crain R. A., Stevens A. R. H., Narayanan D., Saintonge A., Catinella B., Cortese L., 2020, *MNRAS*, 497, 146
- Davies L. J. M., et al., 2018, *MNRAS*, 480, 768
- de Jong R. S., et al., 2019, *The Messenger*, 175, 3
- Delhaize J., Meyer M. J., Staveley-Smith L., Boyle B. J., 2013, *MNRAS*, 433, 1398
- Di Teodoro E. M., Fraternali F., 2014, *A&A*, 567, A68
- Di Teodoro E. M., Fraternali F., 2015, *MNRAS*, 451, 3021
- Driver S. P., et al., 2019, *The Messenger*, 175, 46
- Faucher-Giguère C.-A., Feldmann R., Quataert E., Kereš D., Hopkins P. F., Murray N., 2016, *MNRAS*, 461, L32
- Fernández X., et al., 2016, *ApJ*, 824, L1
- Finoguenov A., et al., 2007, *ApJS*, 172, 182
- Finoguenov A., et al., 2010, *MNRAS*, 403, 2063
- Flaugher B., 2005, *IJMPA*, 20, 3121
- Fraternali F., Oosterloo T., Sancisi R., van Moorsel G., 2001, *ApJL*, 562, L47
- Fraternali F., Binney J. J., 2008, *MNRAS*, 386, 935
- Giovanelli R., et al., 2005, *AJ*, 130, 2598
- Glowacki M., Elson E., Davé R., 2020, *MNRAS*, 498, 3687
- Gupta N., et al., 2016, *Proceedings of MeerKAT Science: On the Pathway to the SKA*. 25-27 May, 14, mks..conf
- Hasinger G., et al., 2018, *ApJ*, 858, 77
- Heald G., et al., 2011, *A&A*, 526, A118
- Healy J., et al., 2019, *MNRAS*, 487, 4901
- Hess K. M., Wilcots E. M., 2013, *AJ*, 146, 124
- Heywood I., et al., 2019, *Natur*, 573, 235
- Hirschauer A. S., et al., 2016, *ApJ*, 822, 108
- Hönig S. F., et al., 2017, *MNRAS*, 464, 1693
- Hoppmann L., Staveley-Smith L., Freudling W., Zwaan M. A., Minchin R. F., Calabretta M. R., 2015, *MNRAS*, 452, 3726
- Huchra J. P., et al., 2012, *ApJS*, 199, 26
- Ilbert O., et al., 2006, *A&A*, 457, 841
- Jaffé Y. L., Poggianti B. M., Verheijen M. A. W., Deshev B. Z., van Gorkom J. H., 2013, *MNRAS*, 431, 2111
- Jaffé Y. L., Smith R., Candlish G. N., Poggianti B. M., Sheen Y.-K., Verheijen M. A. W., 2015, *MNRAS*, 448, 1715
- Jaffé Y. L., et al., 2016, *MNRAS*, 461, 1202
- Jarvis M. J., et al., 2013, *MNRAS*, 428, 1281
- Jarvis M., et al., 2016, *Proceedings of MeerKAT Science: On the Pathway to the SKA*. 25-27 May, 6, mks..conf, arXiv:1709.01901
- Johnston S., et al., 2008, *Experimental Astronomy*, 22, 151
- Jonas J., MeerKAT Team, 2016, *Proceedings of MeerKAT Science: On the Pathway to the SKA*. 25-27 May, 1, mks..conf
- Jones M. G., Hess K. M., Adams E. A. K., Verdes-Montenegro L., 2020, *MNRAS*, 494, 2090
- Jones M. G., Haynes M. P., Giovanelli R., Moorman C., 2018, *MNRAS*, 477, 2
- Jones M. G., et al., 2018, *A&A*, 609, A17
- Jones R. L., Brandt W. N., Cook K. H., Lacy M., Dhital S., LSST Deep Drilling Interest Group, 2013, *AAS*, 221, 247.07
- Kerp J., Winkel B., Ben Bekhti N., Flöer L., Kalberla P. M. W., 2011, *AN*, 332, 637
- Koribalski B. S., Staveley-Smith L., Westmeier T., Serra P., Spekkens K., Wong O. I., Lee-Waddell K., et al., 2020, *Ap&SS*, 365, 118
- Laureijs R. J., Duvet L., Escudero Sanz I., Gondoin P., Lumb D. H., Oosterbroek T., Saavedra Criado G., 2010, *SPIE*, 7731, 77311H, *SPIE*.7731
- Le Fèvre O., et al., 2013, *A&A*, 559, A14
- Leisman L., et al., 2017, *ApJ*, 842, 133
- Lelli F., McGaugh S. S., Schombert J. M., Desmond H., Katz H., 2019, *MNRAS*, 484, 3267
- Lilly S. J., et al., 2009, *ApJS*, 184, 218
- Loeb A., Wyithe J. S. B., 2008, *PhRvL*, 100, 161301
- Maccagni F. M., Morganti R., Oosterloo T. A., Geréb K., Maddox N., 2017, *A&A*, 604, A43
- Maddox N., Hess K. M., Blyth S.-L., Jarvis M. J., 2013, *MNRAS*, 433, 2613
- Maddox N., Hess K. M., Obreschkow D., Jarvis M. J., Blyth S.-L., 2015, *MNRAS*, 447, 1610
- Maddox N., Jarvis M. J., Oosterloo T. A., 2016, *MNRAS*, 460, 3419
- Maddox N., Serra P., Venhola A., Peletier R., Loubser I., Iodice E., 2019, *MNRAS*, 490, 1666
- Mancera Piña P. E., et al., 2019, *ApJL*, 883, L33
- Marasco A., Crain R. A., Schaye J., Bahé Y. M., van der Hulst T., Theuns T., Bower R. G., 2016, *MNRAS*, 461, 2630
- Marasco A., et al., 2019, *A&A*, 631, A50
- Masters K. L., Haynes M. P., Giovanelli R., 2004, *ApJL*, 607, L115
- Mauch T., et al., 2020, *ApJ*, 888, 61
- McGaugh S. S., Schombert J. M., Bothun G. D., de Blok W. J. G., 2000, *ApJL*, 533, L99
- McLure R. J., et al., 2018, *MNRAS*, 479, 25
- McCracken H. J., et al., 2012, *A&A*, 544, A156
- Meyer M., 2009, *Panoramic Radio Astronomy: Wide-field 1-2 GHz Research on Galaxy Evolution*, 15
- Meyer S. A., Meyer M., Obreschkow D., Staveley-Smith L., 2016, *MNRAS*, 455, 3136
- Momcheva I. G., et al., 2016, *ApJS*, 225, 27
- Murphy E. J., et al., 2011, *ApJ*, 737, 67
- Newburgh L. B., et al., 2016, *SPIE*, 9906, 99065X, *SPIE*.9906
- Obreschkow D., Glazebrook K., Kilborn V., Lutz K., 2016, *ApJL*, 824, L26
- Odekon M. C., et al., 2016, *ApJ*, 824, 110
- Crone Odekon M., Hallenbeck G., Haynes M. P., Koopmann R. A., Phi A., Wolfe P.-F., 2018, *ApJ*, 852, 142
- Olivari L. C., Dickinson C., Battye R. A., Ma Y.-Z., Costa A. A., Remazeilles M., Harper S., 2018, *MNRAS*, 473, 4242
- Oman K. A., Marasco A., Navarro J. F., Frenk C. S., Schaye J., Benítez-Llambay A., 2019, *MNRAS*, 482, 821
- Oman K. A., 2019, *ascl.soft*, ascl:1911.005
- Oosterloo T., Fraternali F., Sancisi R., 2007, *AJ*, 134, 1019
- Oosterloo T., Verheijen M. A. W., van Cappellen W., Bakker L., Heald G., Ivashina M., 2009, *Wide Field Astronomy & Technology for the Square Kilometre Array*, 70
- Pan H., et al., 2020, *MNRAS*, 491, 1227
- Papastergis E., Giovanelli R., Haynes M. P., Shankar F., 2015, *A&A*, 574, A113
- Papastergis E., Shankar F., 2016, *A&A*, 591, A58
- Pentericci L., et al., 2018, *A&A*, 616, A174
- Pillepich A., et al., 2018, *MNRAS*, 473, 4077
- Pisano D. J., Wilcots E. M., Liu C. T., 2002, *ApJS*, 142, 161
- Pisano D. J., Barnes D. G., Staveley-Smith L., Gibson B. K., Kilborn V. A., Freeman K. C., 2011, *ApJS*, 197, 28
- Planck Collaboration, et al., 2018, *arXiv*, arXiv:1807.06209
- Ponomareva A. A., Verheijen M. A. W., Bosma A., 2016, *MNRAS*, 463, 4052
- Ponomareva A. A., Verheijen M. A. W., Peletier R. F., Bosma A., 2017, *MNRAS*, 469, 2387
- Ponomareva A. A., Verheijen M. A. W., Papastergis E., Bosma A., Peletier R. F., 2018, *MNRAS*, 474, 4366
- Posti L., Fraternali F., Di Teodoro E. M., Pezzulli G., 2018, *A&A*, 612, L6
- Putman M. E., Peek J. E. G., Jong M. R., 2012, *ARA&A*, 50, 491
- Rafieferantsoa M., Davé R., 2018, *MNRAS*, 475, 955
- Rafieferantsoa M., Davé R., Naab T., 2019, *MNRAS*, 486, 5184
- Rhee J., Lah P., Chengalur J. N., Briggs F. H., Colless M., 2016, *MNRAS*, 460, 2675
- Rhee J., et al., 2018, *MNRAS*, 473, 1879
- Robotham A. S. G., Davies L. J. M., Driver S. P., Koushan S., Taranu D. S., Casura S., Liske J., 2018, *MNRAS*, 476, 3137
- Said K., Kraan-Korteweg R. C., Staveley-Smith L., 2019, *MNRAS*, 486, 1796
- Sancisi R., Fraternali F., Oosterloo T., van der Hulst T., 2008, *A&ARv*, 15, 189
- Santos M., et al., 2015, *Advancing Astrophysics with the Square Kilometre Array (AASKA14)*, 19
- Santos M. G., et al., 2017, *arXiv*, arXiv:1709.06099
- Schaye J., et al., 2015, *MNRAS*, 446, 521
- Schönrich R., Binney J., 2009, *MNRAS*, 396, 203
- Serra P., et al., 2013, *MNRAS*, 428, 370
- Serra P., et al., 2015, *MNRAS*, 448, 1922
- Serra P., et al., 2016, *Proceedings of MeerKAT Science: On the Pathway to the SKA*. 25-27 May, 8, mks..conf, arXiv:1709.01289
- Shetty R., Ostriker E. C., Vogel S. N., 2008, *AAS*, 212, 92.02
- Silverman J. D., et al., 2015, *ApJS*, 230, 12
- Skelton R. E., et al., 2014, *ApJS*, 214, 24
- Skillman E. D., et al., 2013, *AJ*, 146, 3
- Skrutskie M. F., et al., 2006, *AJ*, 131, 1163
- Somerville R. S., Davé R., 2015, *ARA&A*, 53, 51
- Switzer E. R., et al., 2013, *MNRAS*, 434, L46
- Tiley A. L., et al., 2019, *MNRAS*, 482, 2166
- Topal S., Bureau M., Tiley A. L., Davis T. A., Torii K., 2018, *MNRAS*, 479, 3319
- Tully R. B., Fisher J. R., 1977, *A&A*, 500, 105
- Übler H., et al., 2017, *ApJ*, 842, 121
- van der Kruit P. C., 2007, *A&A*, 466, 883
- Venhola A., et al., 2018, *A&A*, 620, A165
- Verbeke R., Papastergis E., Ponomareva A. A., Rath S., De Rijcke S., 2017, *A&A*, 607, A13
- Verdes-Montenegro L., et al., 2005, *A&A*, 436, 443
- Verheijen M. A. W., Oosterloo T. A., van Cappellen W. A., Bakker L., Ivashina M. V., van der Hulst J. M., 2008, *AIPC*, 265, AIPC.1035
- Verheijen M., van Gorkom J. H., Szomoru A., Dwarakanath K. S., Poggianti B. M., Schiminovich D., 2007, *ApJL*, 668, L9
- Vogelsberger M., et al., 2014, *MNRAS*, 444, 1518
- Wang J., et al., 2015, *MNRAS*, 453, 2399
- Wang J., Koribalski B. S., Serra P., van der Hulst T., Roychowdhury S., Kamphuis P., Chengalur J. N., 2016, *MNRAS*, 460, 2143
- Watts A. B., Catinella B., Cortese L., Power C., 2020, *MNRAS*, 492, 3672
- Willick J. A., 1999, *ApJ*, 516, 47
- Wolz L., Abdalla F. B., Blake C., Shaw J. R., Chapman E., Rawlings S., 2014, *MNRAS*, 441, 3271
- Wolz L., Blake C., Wyithe J. S. B., 2017, *MNRAS*, 470, 3220
- Wong O. I., et al., 2006, *MNRAS*, 371, 1855
- Xu Y., Wang X., Chen X., 2015, *ApJ*, 798, 40
- Yoon I., Rosenberg J. L., 2015, *ApJ*, 812, 4
- Yoon H., Chung A., Smith R., Jaffé Y. L., 2017, *ApJ*, 838, 81